JOURNAL OF AIRCRAFT
Vol. 63, No. 3, May–June 2026

Slipstream Deformation in Propeller–Wing–Flap Aerodynamic Interaction

Ramon R. Duivenvoorden,* André F. P. Ribeiro,† Tomas Sinnige,‡ and Leo L. M. Veldhuis§
Delft University of Technology, 2629 HS Delft, The Netherlands

https://doi.org/10.2514/1.C038435

Propeller–wing–flap configurations exhibit highly complex flow patterns due to the aerodynamic interactions among their components. To facilitate effective design of such configurations, a fundamental understanding of these interactions is essential. This paper characterizes the deformation of a propeller slipstream caused by nacelle, wing, and flap interference at various angles of attack and flap deflections, based on validated numerical simulations. We examine different stages and mechanisms of deformation, from immediately behind the propeller to the wake downstream of the wing. Our findings reveal that significant deformation occurs in high-lift conditions before the slipstream physically interacts with the wing, profoundly impacting subsequent deformation. Furthermore, the root vortex system rolls into a strong nacelle vortex that induces crossflow on the wing surface behind the nacelle and dominates the slipstream deformation in the wake. Additionally, the tip vortices stretch around the leading edge and roll into vortex systems aligned with the wing surface, dominating local flow features. These insights improve the understanding of slipstream deformation, helping to improve the aerodynamic performance of propeller–wing–flap systems.

I. Introduction

IN THE context of a net-zero emissions aviation sector, industry and academia alike have committed to the resurgence of propeller technology. In particular, innovative propeller–airframe integration such as distributed propulsion and high-lift propeller systems has gained favor, spearheaded by the advent of electric motors for aviation applications. Consequently, propeller–wing aerodynamic interaction will have a prominent role in next-generation aircraft performance. Particularly the focus on synergistic propeller–wing integration requires a thorough understanding of PWI and the aerodynamic phenomena involved.

As the slipstream interacts with the wing, it deforms and displaces in the spanwise direction [1–3]. This deformation varies strongly between low and high lift conditions, and for a flapped wing, it has a significant impact on which part of the flap is immersed in the slipstream [4]. Furthermore, the slipstream interaction with downstream surfaces such as the empennage is critical to aircraft control and stability [5,6], which is also dependent on the slipstream deformation. In order to extract aerodynamic benefits from the propeller–wing(–flap) interaction, understanding the slipstream deformation and the aerodynamic mechanisms by which it occurs is therefore critical.

Although the basic principles of propeller–wing aerodynamic interaction are well understood from fundamental works such as Prandtl [7], Jameson [8], and Witkowski et al. [9], they describe the interaction mainly in terms of performance coefficients of the wing and propeller. Insight into the fluid dynamics of the propeller slipstream interacting with the wing is limited. Moreover, these works are mostly focused on the cruise condition and do not feature flapped wings. Roosenboom [10–12] does shed light on the internal structure of the slipstream as it passes the wing in a high-lift transport aircraft configuration but does not extend their analysis to the flap region. They also focus on streamwise slices of the slipstream, which do not visualize the spanwise extent of the slipstream deformation.

A separate body of work exists on slipstream deflection by multi-element wings with the goal of achieving fixed-wing vertical takeoff and landing (VTOL) capability (e.g., Kuhn and Draper [13], Kuhn and Hayes [14], Hayes et al. [15], and Newsom [16]). These include extensive wind tunnel measurements of aerodynamic coefficients and slipstream turning ratio for various propeller positions and flap deflections. However, they again provide little information in terms of the development of the actual flow around the wing. Additionally, they often feature complex designs with multiple slats, flaps, and vanes at very high deflection angles to maximize the slipstream turning ratio. This makes it difficult to transfer the results to the simpler, single-flap configurations favored in modern aircraft design.

While the underlying mechanisms of slipstream deformation have not been fully studied in aeronautical literature, substantial work has been done in the related field of propeller–rudder interaction. Felli et al. [17] and Felli and Falchi [18] performed extensive experimental measurements of a propeller–rudder configuration using particle image velocimetry (PIV) and laser Doppler velocimetry (LDV). They discuss the dynamics of the tip and hub vortices of a propeller slipstream as they encounter a downstream rudder, showing that the tip vortices wrap around the rudder (or wing) leading edge and maintain connection between the tip vortices on both sides of the wing until they leave the trailing edge. They also propose the main mechanisms of slipstream deformation to be a combination of vortex image effects and spanwise pressure gradients displacing the tip vortices at the edge of the slipstream. Felli and Falchi [18] furthermore show that the hub vortex has a profound interaction with the boundary layer when it impinges on the wing directly and experiences a spanwise shift opposite to that of the tip vortices. Felli et al. [17] report no such interaction, as their propeller is offset from the wing and the hub vortex passes the wing away from the surface.

The dynamics of the tip and hub vortices is further investigated by Muscari et al. [19] using detached eddy simulation. They note that the interaction cannot be treated as separate mechanisms of tip and hub vortex impingement, as they strongly affect each other as well. Additionally, they stress the importance of the exchange of vorticity between the slipstream and the wing boundary layer. Felli [3] continues the work of Felli and Falchi [18] and Muscari et al. [19], providing a very thorough overview of the dynamics of the

This paper is related to two previous AIAA conference presentations: Paper 2022-3216, AIAA Aviation Forum 2022, Chicago, IL, June 27–July 1, 2022, and Paper 2023-3541, AIAA Aviation Forum 2023, San Diego, CA, June 12–16, 2023; received 18 February 2025; accepted for publication 11 August 2025; published online 24 October 2025.

*Ph.D. Candidate, Faculty of Aerospace Engineering; r.r.duivenvoorden@tudelft.nl.
†Ph.D. Candidate, Faculty of Aerospace Engineering.
‡Assistant Professor, Faculty of Aerospace Engineering.
§Full Professor, Faculty of Aerospace Engineering.

slipstream vortex system as it interacts with a rudder, based on another extensive experimental campaign. Posa et al. [20] perform large-eddy simulations (LESs) of the configuration tested by Felli and Falchi [18] and are able to characterize the slipstream deformation in additional detail, confirming the mechanisms described by Felli and Falchi [18] and Muscaria et al. [19]. Posa and Broglia [21,22] later extend the state-of-the-art with simulations of a propeller–rudder configuration with a rudder at incidence, providing extensive descriptions of the flowfield, although they do not analyze the vortex dynamics and mechanisms to the extent that Felli [3] does for the zero incidence case.

Despite the extensive work on the dynamics of the helical vortex system in propeller–rudder interaction, there are several important differences with a typical aeronautical application that require addressing before a direct translation of the results can be made. Firstly, all works on propeller–rudder interaction discussed thus far share the same propeller and model topology. Additionally, most of the works consider a nonlifting wing, which is not the operating condition of interest for aeronautical applications. The studies by Posa and Broglia [21,22] are an exception, as they address the impact of a rudder at incidence. However, the angle of attack is only applied to the wing, while the propeller keeps the same orientation. This is not representative of an installed tractor propeller on an aircraft for two reasons: it effectively changes the position of the propeller relative to the airfoil, and it avoids a substantial part of the nonuniform inflow field that the propeller will experience when it is tilted together with the wing. Furthermore, the propeller in the aforementioned works is always detached, which may lead to different hub vortex dynamics and wing interaction compared to an attached nacelle. The nacelle–wing junction will also affect the propeller–wing interaction in aeronautical applications, as it induces local suction peaks on the wing leading edge [23] and may result in local separation bubbles [24]. Finally, a slotted flap element has never been considered before, which also limits the levels of wing circulation that have been included in literature thus far. It is therefore worthwhile to characterize the slipstream of a given propeller–wing–flap configuration, study its development from the initial circular shape, and compare this to established literature.

In this paper, we therefore characterize the development of the slipstream for an aeronautical propeller–wing–flap configuration. This configuration features an asymmetric wing profile, a leading-edge-mounted nacelle, and a deployable Fowler flap. We visualize the slipstream shape from just behind the propeller up to the far wake and discuss how it deforms and how this compares with established literature. We analyze the interaction of the tip and root vortex systems with the leading edge and show how they roll up and dominate local flow features. Furthermore, instability of the helical vortex structure in high-lift conditions is discussed, showing the difference between the slipstream interactions of the main and flap elements.

The analyses in this paper are based on previously validated numerical simulations. The original experiment that serves as validation data was described in [4], while the numerical setup and validation were discussed in [25]. The current paper fully covers the analysis described in those papers and expands significantly on this analysis in terms of flowfield dynamics, slipstream deformation, and discussions of underlying aerodynamic mechanisms. In the current work, we fully leverage the benefits of validated high-fidelity numerical data to further explore aerodynamic phenomena of the propeller–wing–flap interaction that could not be explored in detail based on the experimental data alone. While we only investigate a single propeller–wing–flap design, we reflect (and expand) on how mechanisms from literature (e.g., Felli [3]) apply to an aeronautical configuration in a manner that can be intuitively transferred to different propeller–wing geometries.

II. Methods

This paper presents a comprehensive analysis combining both experimental and numerical data. The primary focus lies in the detailed analysis of numerical data, expanded with experimental data where necessary. The numerical simulations were conducted with the lattice Boltzmann solver PowerFLOW®. In this paper, we will shortly summarize the employed methods and experimental validation. However, the reader is referred to the original works for full details on the experiment [4] and the numerical setup and validation [25].

A. Experimental Setup

The experiment was performed in the Low Turbulence Tunnel of the Delft University of Technology. The experimental setup consisted of an unswept, wall-to-wall mounted wing model with an NLF-mod22(B) airfoil [26], featuring a 0.3 m chord and 1.25 m wingspan. This model was equipped with a deployable Fowler flap system and featured a single propeller ($D_{\text{prop}} = 0.2032$ m, $\beta_{0.7R} = 30$ deg) on the wing centerline. The propeller model is TUD-XPROP-S, the geometry of which is available from [27], while its performance is described in [28]. The propeller was mounted to the wing by a nacelle that attaches to the leading edge at a downward angle of 5 deg with respect to the wing chord. The wing boundary layer was tripped by a zigzag strip at $0.1c$ on the main element suction side only. The model setup is illustrated in Fig. 1, while Fig. 2 shows a technical drawing of the model. Note the orientation of the reference axes, where the x-coordinate is defined as positive upstream.

Tests were conducted at $V_\infty = 30$ m/s, exploring three flap deflections (0, 15, and 30 deg) at various angles of attack (0 and 8 deg are used in this paper). The propeller was operating at $J = 0.8$ ($T_c = 1.05$, where $T_c = T/\rho V^2 D^2$). Measurement techniques included two chordwise rows of pressure taps, positioned at $y/R = \pm 0.7$, a wake rake with total and static pressure probes positioned downstream at $x/c = -2$,[¶] and oil flow visualization on the wing suction side. Each measurement technique was employed individually to avoid interference effects. The experimental dataset, along with additional measurements from other experiments with the same model geometry, is available at [29].

B. Numerical Setup

Numerical simulations were performed in PowerFLOW® (version 6-2021-R7), a commercial CFD code that employs the lattice Boltzmann method (LBM). LBM is based on statistical mechanics and represents fluid flow as interacting particles. The Boltzmann equation governs the behavior of the particle distribution function, akin to the Navier–Stokes (N-S) equations with time derivatives and advection terms. Specifically, the D3Q19 formulation is utilized, discretizing the particle velocities into 19 vectors, allowing particles to travel to adjacent cells.

Simulations were conducted using the subsonic isothermal solver and very-large-eddy simulation (VLES) approach. This employs a κ–ε renormalization group (RNG) turbulence model with a swirl model to reduce the eddy viscosity in the presence of resolved flow structures. The numerical setup involved a Cartesian mesh with variable cell sizes, refined near the propeller wake and flap surfaces. This mesh setup included a sliding mesh interface for propeller rotation, with a refined cylinder around the propeller wake to mitigate numerical dissipation. An illustration of mesh refinement regions near the wing is presented in Fig. 3. The wind tunnel walls, simulated as free-slip boundaries, were included to eliminate the need for wall corrections. The propeller and wing surfaces were included with a no-slip condition and fully turbulent boundary-layer flow. Furthermore, the flap brackets used to mount the flap to the main element were also included, as they locally dominate the flap flow. The CAD files of the wind tunnel model geometry, as used in the numerical simulations, are available at [30]. Boundary conditions consisted of a velocity inlet and a pressure outlet at the upstream and downwind faces of the numerical wind tunnel, respectively. The numerical dataset includes six configurations, consisting of two angles of attack ($\alpha = 0$ and 8 deg) and three flap deflections

[¶]Again, the x-coordinate is defined as positive upstream.

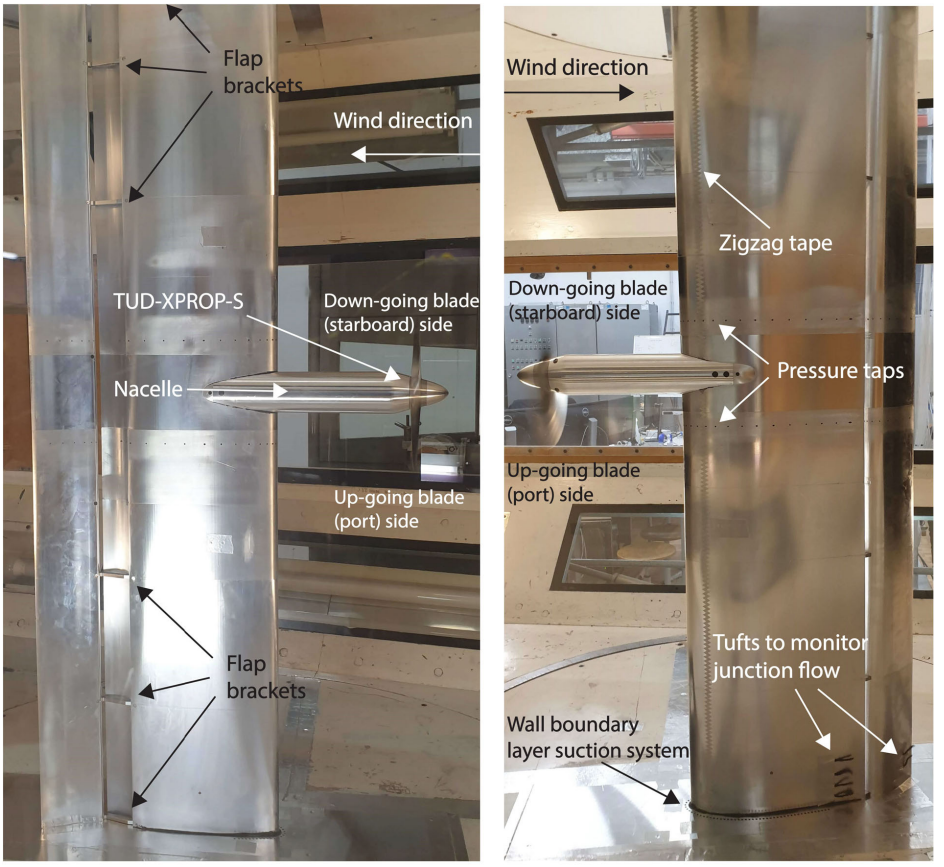

a) Pressure side b) Suction side

Fig. 1 Wing as placed in the test setup with flap deployed and nacelle and prop attached. From [4].

(0, 15, and 30 deg), matching the experiment. Each configuration considered only one advance ratio of $J = 0.8$.

C. Verification and Validation

The numerical results were validated using the experimental data in [25], showing excellent agreement overall. We include some parts of this validation here for the benefit of the reader. This includes an indication of grid convergence based on thrust coefficient, comparisons of local pressure measurements on the wing, and distributions of total pressure in the wake of the wing. The latter is an effective comparison of the entire aerodynamic system, as the slipstream deformation in the wake is the result of all upstream aerodynamic interactions. To arrive at the same deformation in the wake, the various mechanisms of deformation and interactions that occur between the propeller plane and the wake plane have to be modeled accurately.

The interested reader is referred to the original validation paper [25] for additional comparisons, which are not included in this paper for brevity. It contains additional comparisons of wing pressures and total pressure distributions, qualitative comparisons of numerical wing shear with experimental oil flow visualization, and a short study of boundary-layer transition effects. Unfortunately, the experimental dataset only includes time-averaged data, and thus the time-accurate results of the numerical dataset are not validated separately. Most analyses in this paper are confined to the time-averaged values, but we do use the time-accurate results to deepen our analyses. This is then done under the assumption that the time-accurate results represent the actual flow with adequate accuracy.

1. *Grid Convergence*

Experiments by van Arnhem et al. [28] yield the thrust coefficient of TUD-XPROP-S at $J = 0.8$ and $\alpha = 0$ deg in isolated conditions. We can use this as an approximate reference for our simulations and concurrently verify if the propeller thrust achieved in CFD is grid convergent. Note that since the simulations feature the propeller in installed conditions, the thrust coefficient is expected to deviate slightly. The values of T_c for the three resolutions simulated at $\delta_f = 30$ deg, $\alpha = 8$ deg are shown in Table 1, together with the experimental reference value. This combination of flap and wing angle settings was chosen as they feature the most complex aerodynamic features, under the assumption that convergent behavior for this case will be representative for the less complex cases also.

Grid convergent behavior is observed, with the difference between the fine and medium grids being over two times smaller than the difference from medium to coarse. The value of T_c is within 1% of the reference for the isolated propeller, which we consider adequate given also the difference in installation configuration between the numerical simulation and reference data.

Figure 4 compares the experimental chordwise pressure distributions with the simulated results for three grid resolutions. Again, we select the highest flap deflection and angle of attack in our simulations, as it represents the most challenging case. Figure 4 shows that the smooth body separation over the flap is slightly affected by the resolution, in particular on the downgoing blade side, but the results do not change substantially with an increase in grid resolution. Hence, we decided to use the medium resolution for all results presented in this paper.

The original validation by Ribeiro et al. [25] also featured an exploration of the impact of transition on the flap. This is not included in the present paper for the sake of brevity. Applying a transition model slightly improved agreement but was ultimately not adopted for the remaining simulations to avoid the uncertainties associated with transition models for high-lift configurations [31]. The results in this paper thus feature no transition model but rather assume fully turbulent boundary layers on all components of the tested geometry.

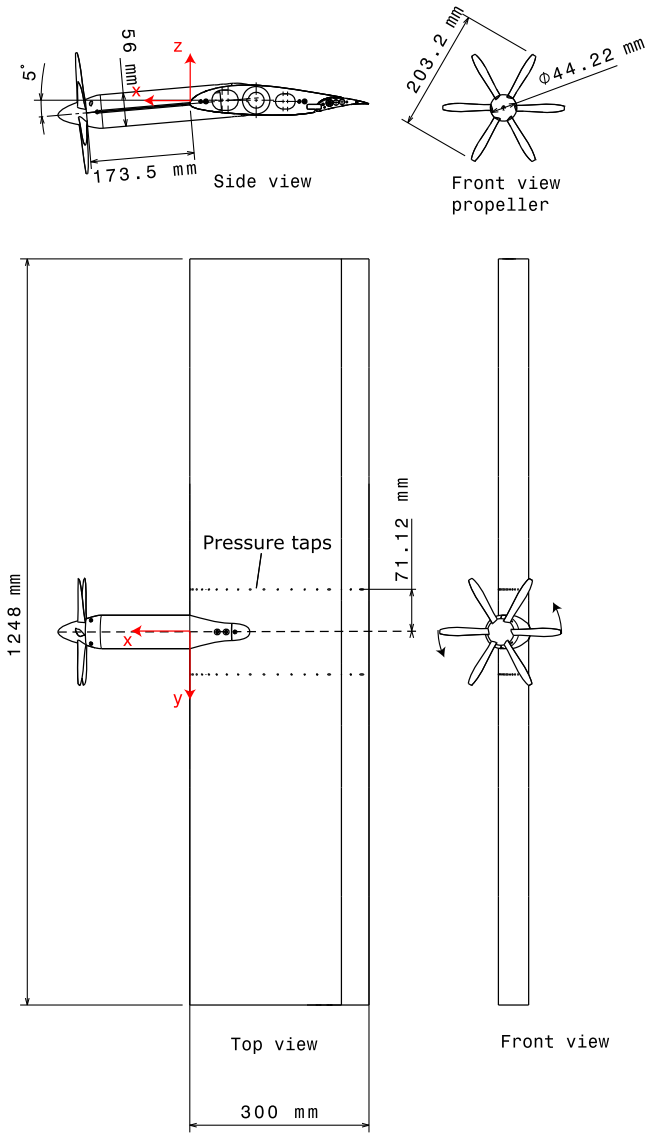

Fig. 2 Technical drawing of wind tunnel model.

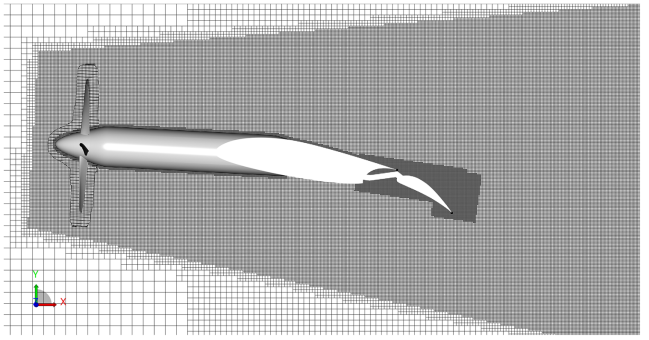

Fig. 3 Illustration of the mesh refinement areas, also showing the sliding mesh region around the propeller. From [25].

2. Comparison of Pressure Distributions on the Wing and in the Wake

Figure 5 shows a comparison of local chordwise pressure distributions from experimental measurements and numerical results. All results show good agreement with the experiment. However, for $\delta_f = 30$ deg, the simulations show discrepancies compared to experiments in the suction peaks, which is attributed to laminar-to-turbulent transition and to significant flow separation on the flap (see [25] for more details). We therefore confine the analyses in this paper to the configurations with $\delta_f = 0$ deg and $\delta_f = 15$ deg. The $\delta_f = 15$ deg configuration displays mostly the same aerodynamic phenomena as the $\delta_f = 30$ deg configuration (although less pronounced), without raising doubts on the accuracy of the simulations.

Table 1 Thrust coefficients for different grid resolutions at $\delta_f = 30$ deg, $\alpha = 8$ deg, and experimental value for isolated propeller at $\alpha = 0$ deg (from [25])

Resolution	T_c
Coarse	0.405
Medium	0.408
Fine	0.409
Experiment	0.412

Figure 6 presents an additional point of comparison based on the distribution of the total pressure coefficient $C_{p,t} = p_t - p_{s,\infty}/q_\infty$ in the wake of the wing. For the aforementioned reasons, we only include the configurations with $\delta_f = 0$ and 15 deg here. Additional comparisons of the total pressure distributions, including those for the $\delta_f = 30$ deg configurations, can be found in [25]. The experimental results in Fig. 6 are based on wake rake measurements with an effective resolution of ≤ 3 mm in the z-direction (resulting from overlap of the nonuniformly spaced probes of the rake) and 10 mm in the y-direction. The contours were generated using the *ScatteredInterpolant* method in MATLAB.

The experimental and numerical results show good agreement in terms of slipstream shape and the distribution of total pressure coefficient, which can be interpreted as a result of the upstream aerodynamic system. Whereas traditional N-S solvers often struggle to resolve the slipstream downstream of the wing due to the dissipation and diffusion of vorticity, the LBM solver used in this study was able to capture the slipstream deformation relatively accurately. This lends further confidence in the accuracy of the numerical results, particularly for the analyses of slipstream deformation in this paper.

III. Results and Discussion

In this section, we use the validated numerical results to investigate the physics of propeller–wing–flap interaction. As mentioned in the previous section, this only includes the configurations with $\delta_f = 0$ and 15 deg, as they showed the best agreement with experimental data. We shortly analyze the wing lift distribution of the main and flap elements, illustrating the relevance of slipstream deformation to aerodynamic performance. Subsequently, we visualize the slipstream deformation upstream of the wing, over the wing, and in the wake, and discuss by which mechanisms these deformations occur.

A. On the Relevance of Slipstream Deformation

Figure 7 shows the spanwise distribution of sectional lift coefficients for the main and flap elements. Horizontal dashed lines represent the sectional lift coefficient of the clean wing, estimated by taking the average of the lift coefficient between $y/R = -6$ and -4. The distributions are calculated from numerical simulations by integrating the force over finite spanwise sections of the main wing and flap element surfaces. Since the nacelle is blended into the wing, their individual contributions cannot be properly separated. The lift distributions in Fig. 7 therefore include the nacelle contribution. As a result, the sectional lift coefficients in the nacelle region are not representative of the wing performance and are therefore reported with dotted lines.

The results in Fig. 7 show distinct differences in how the main and flap elements are affected by the slipstream as a result of its deformation. Under the influence of the propeller slipstream, the lift distribution on the wing changes. On the main element, most of this change is located within the area directly behind the propeller. The distribution is asymmetric around the wing center axis due to the effects of swirl, and the strongest gradient is found on the upgoing blade side. The gradients in spanwise lift cause shedding of trailing vorticity, which induces increased wing lift on the upgoing blade side. This effect extends beyond the wing area directly behind the propeller. These effects all follow standard propeller–wing interaction theory known from, e.g., Veldhuis [2]. The flap lift distribution, however, shows

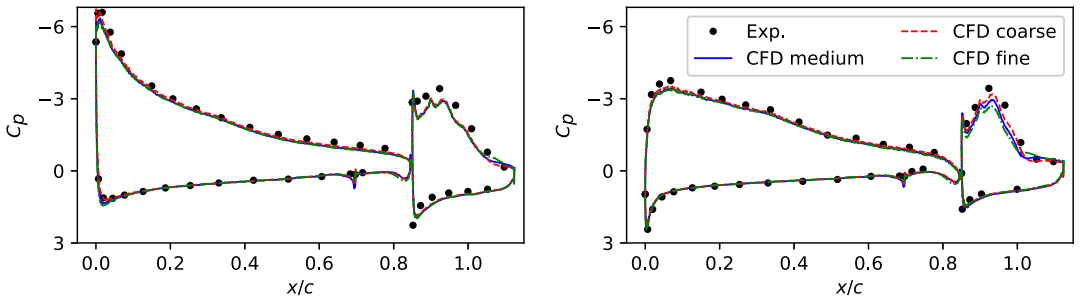

a) Upgoing blade side **b) Downgoing blade side**

Fig. 4 Effect of grid resolution on pressure coefficient along the wing chord for $\delta_f = 30$ deg, $\alpha = 8$ deg. From [25].

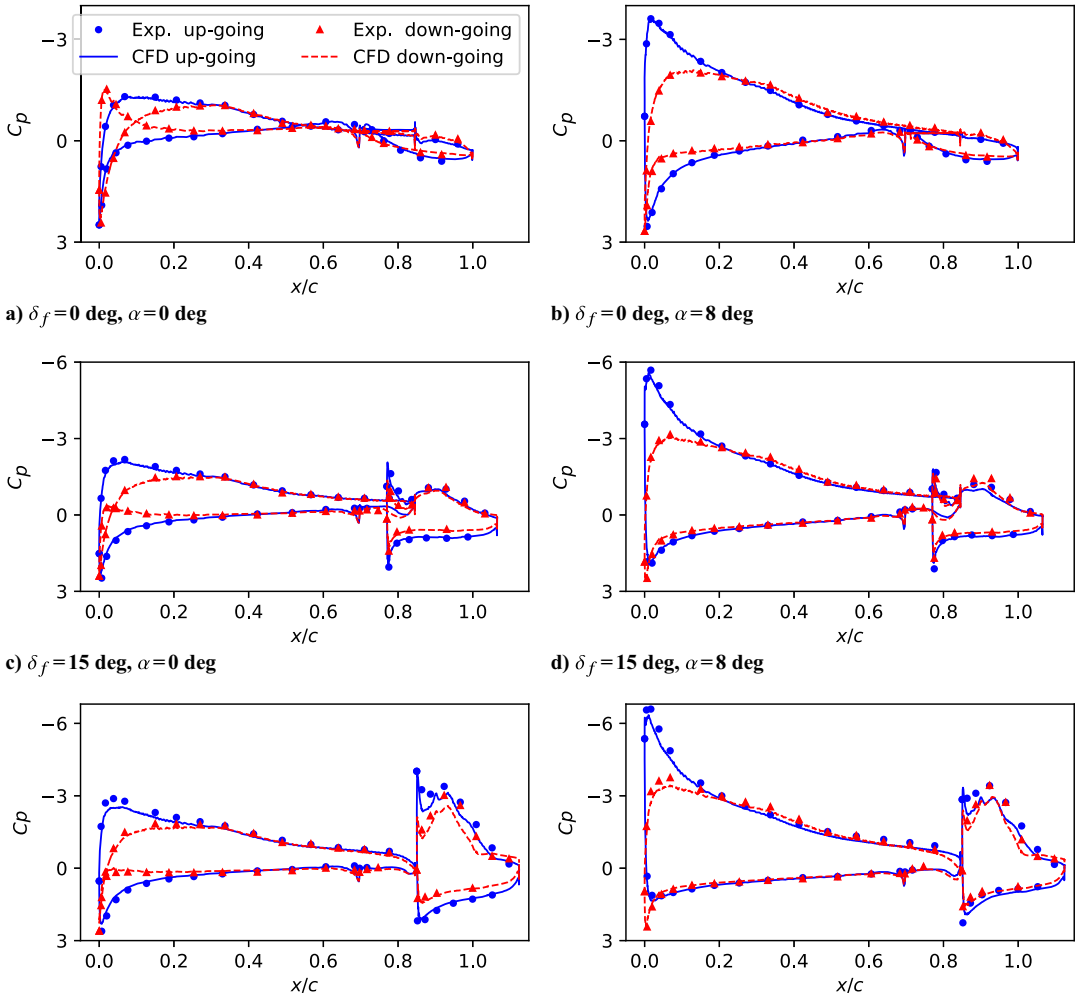

a) δ_f=0 deg, α=0 deg **b) δ_f=0 deg, α=8 deg**

c) δ_f=15 deg, α=0 deg **d) δ_f=15 deg, α=8 deg**

e) δ_f=30 deg, α=0 deg **f) δ_f=30 deg, α=8 deg**

Fig. 5 Pressure coefficient along the wing chord on the upgoing and downgoing blade sides of the propeller for various flap angles δ_f and angles of attack α. From [25].

some very distinct differences. Mainly, the distribution is no longer strongly asymmetric, suggesting that the flap does not experience a swirling flow, which would induce spanwise variation of apparent angle of attack. The lift augmentation on the flap is also shifted toward the upgoing blade side to varying degrees. This can be attributed to the deformation of the slipstream on the lower surface of the main element, as was demonstrated by the authors in previous work [4,25].

It should be noted that the lift of multi-element wings is the result of a fully coupled aerodynamic system, meaning that the lift distributions of the main and flap elements cannot be truly analyzed separately. For example, the augmentation of the flap lift will induce additional circulation on the main element as well [32]. Nevertheless, understanding the aerodynamic phenomena by which the slipstream interacts with the wing and flap, and especially how these interactions differ from each other, can assist in optimizing the overall wing performance.

B. Regions of Deformation

The propeller–wing–flap aerodynamic interaction distorts and deforms the propeller slipstream in various ways as it moves past the wing. The development of the slipstream shape shown in Fig. 8, visualizing the outline of the slipstream by means of the contour line of $C_{p,t} \geq 1.05$. This value is chosen to get a clear visualization of the slipstream edge. As the propeller adds total pressure to the flow, the slipstream can be defined by this increase in total pressure.

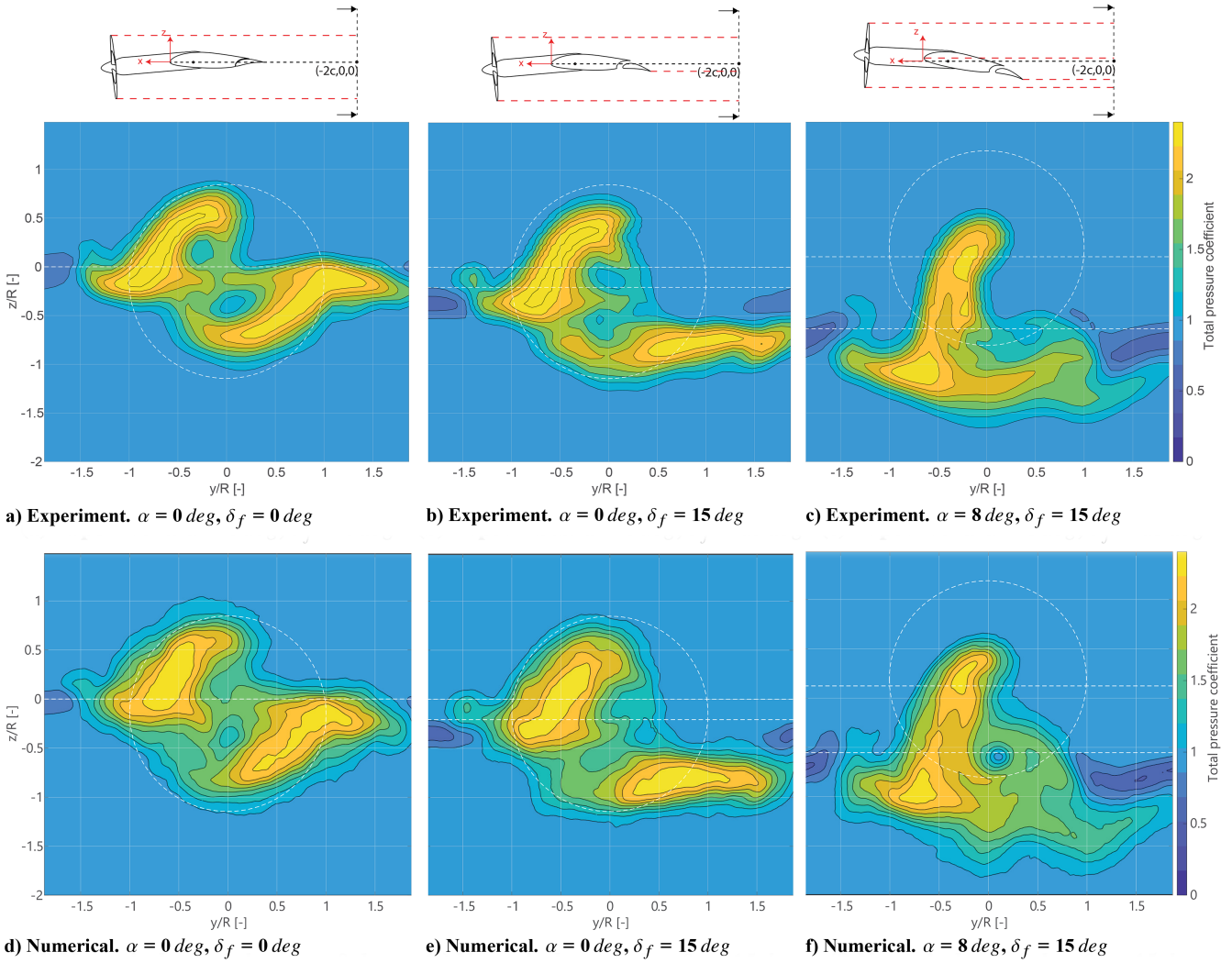

a) Experiment. $\alpha = 0\,deg, \delta_f = 0\,deg$ **b) Experiment.** $\alpha = 0\,deg, \delta_f = 15\,deg$ **c) Experiment.** $\alpha = 8\,deg, \delta_f = 15\,deg$

d) Numerical. $\alpha = 0\,deg, \delta_f = 0\,deg$ **e) Numerical.** $\alpha = 0\,deg, \delta_f = 15\,deg$ **f) Numerical.** $\alpha = 8\,deg, \delta_f = 15\,deg$

Fig. 6 Slices of total pressure coefficient $C_{p,t}$ in the wake of the wing at $x/c = -2$ from experimental measurement (top) and numerical simulation (bottom). From [25].

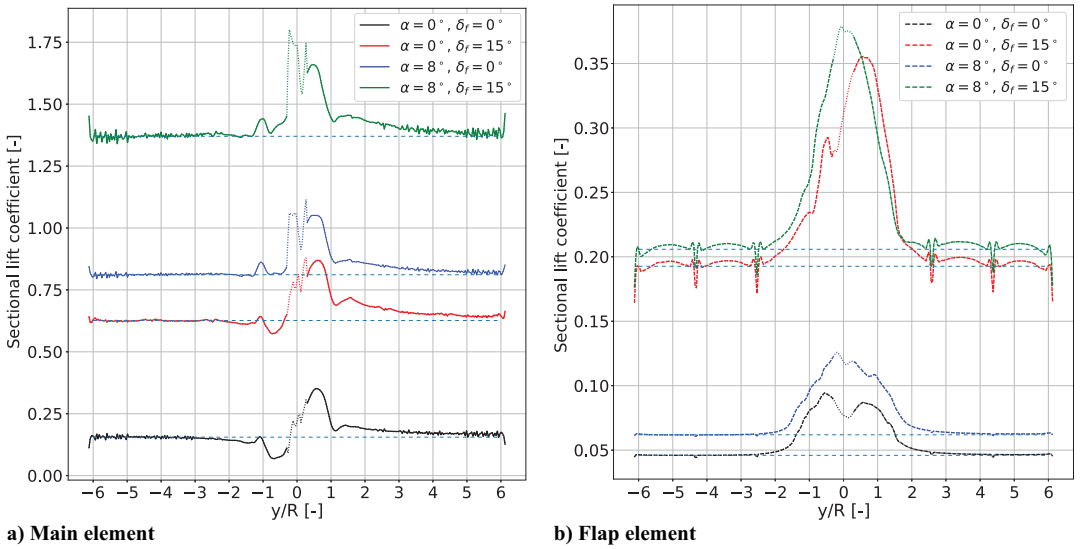

a) Main element **b) Flap element**

Fig. 7 Spanwise lift distributions for the main and flap elements, extracted from the numerical simulations. Horizontal dashed lines indicate the sectional wing lift without influence of the propeller.

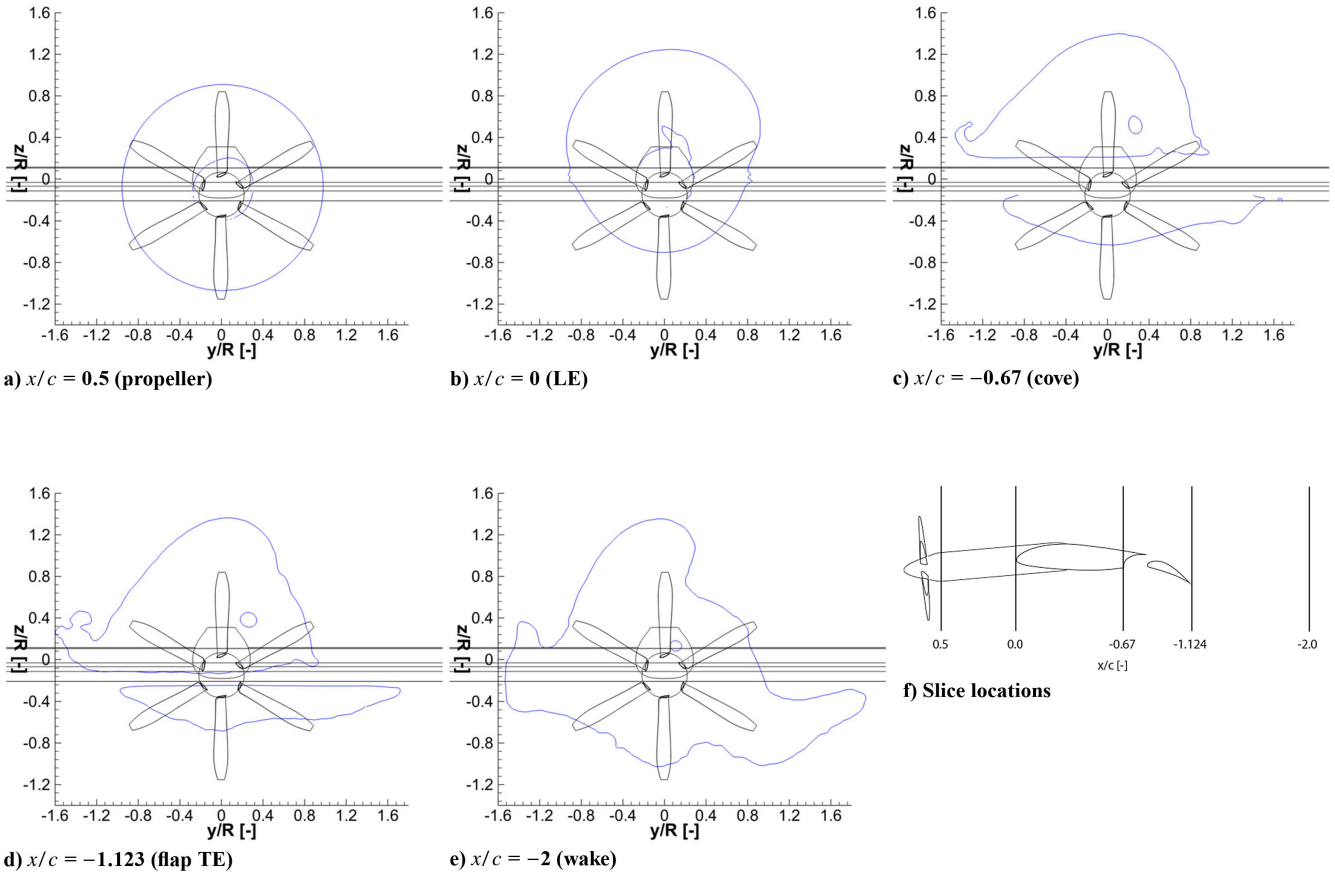

a) $x/c = 0.5$ **(propeller)** **b)** $x/c = 0$ **(LE)** **c)** $x/c = -0.67$ **(cove)**

f) Slice locations

d) $x/c = -1.123$ **(flap TE)** **e)** $x/c = -2$ **(wake)**

Fig. 8 Contour lines of $C_{P,t} = 1.05$ at various downstream stations illustrating overall slipstream deformation.

However, due to measurement noise and viscous effects, the slipstream edge is diffused. The contour line at $C_{p,t} = 1$ therefore becomes irregular. Since the gradient in total pressure at the slipstream boundary is very steep, we can instead take the contour line of $C_{p,t} = 1.05$ as a good representation of the position of the slipstream edge. This provides an effective visualization of the slipstream shape while mitigating the effects of noise and viscous losses on the clarity of the contours.

Figure 8 shows the slipstream shape at various streamwise locations: upstream of the wing, at the main element leading edge, at the main element cove, and in the wing wake, for the case with $\alpha = 8$ deg and $\delta_f = 15$ deg. Figure 8f visualizes the locations of the slices. From Fig. 8, it becomes clear that significant slipstream deformation occurs not only when the slipstream physically intersects with the wing surface but also upstream and downstream of the wing.

To further analyze the development of the slipstream deformation, we define three regions, shown in Fig. 9. Note that the first region is aligned with the propeller axis, while the other two regions are aligned with the wing chord. For any of these regions, the flow is a result of the coupled interaction between propeller and wing. The slipstream affects the local wing aerodynamics, while the wing affects the slipstream trajectory and the propeller performance, which in turn affects the distribution of total pressure in the slipstream. This can never be treated as anything but the complete sum of its parts. In the next sections, we discuss the different phenomena that deform the slipstream sequentially in the streamwise direction, knowing that we are describing the complete end result only.

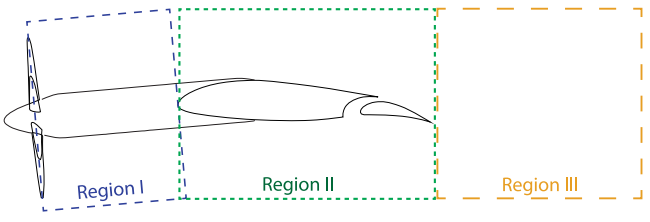

Fig. 9 Definition of slipstream deformation analysis regions.

C. Region I: Propeller to Wing

Figure 10 shows contours of total pressure coefficient in a plane just behind the propeller, combined with the in-plane components of the velocity vectors (hereinafter referred to as the *in-plane velocity vectors*). At this position, the slipstream is in its initial state. We define this region in the propeller frame, with the yz-plane parallel to the plane of rotation, to best visualize the deformation from the initial circular shape.

The initial state of the slipstream is inherently a function of both the angle of attack and the wing upwash. At $\alpha = 0$ deg and no flap deflection, the propeller sees a slight negative angle of inflow (meaning a negative z-component), as the wing-induced upwash is insufficient to offset the negative geometric angle of the propeller with respect to the wing chord. This results in a slightly higher concentration of $C_{p,t}$ on the upgoing blade side of Fig. 10a (positive y/R). Deflecting the flap to 15 deg (Fig. 10b) increases the wing circulation enough to counteract the geometric installation angle, and the propeller operates nearly in uniform flow conditions, evident from the nearly axisymmetric $C_{p,t}$ distribution. The propeller thus experiences a significant effect of the wing upwash, even at $\alpha = 0$ deg. Also note that the configuration has a relatively long nacelle and thus less wing-induced upwash at the propeller plane than a typical configuration.

For higher angles of attack (Figs. 10c and 10d), the propeller operates at a positive relative inflow angle. This results in a concentration of total pressure on the downgoing blade side. The blade sees an in-plane component of the inflow velocity, which moves against the downgoing blade and with the upgoing blade. We can denote these sides as the advancing and retreating blade sides, respectively. As a result of the in-plane velocity component, the maximum pressure rise shifts to the downgoing (advancing) blade side. These effects are all well described by the classic works on propeller–wing interaction (e.g., Veldhuis [2]) and further investigated by Stokkermans [33] and

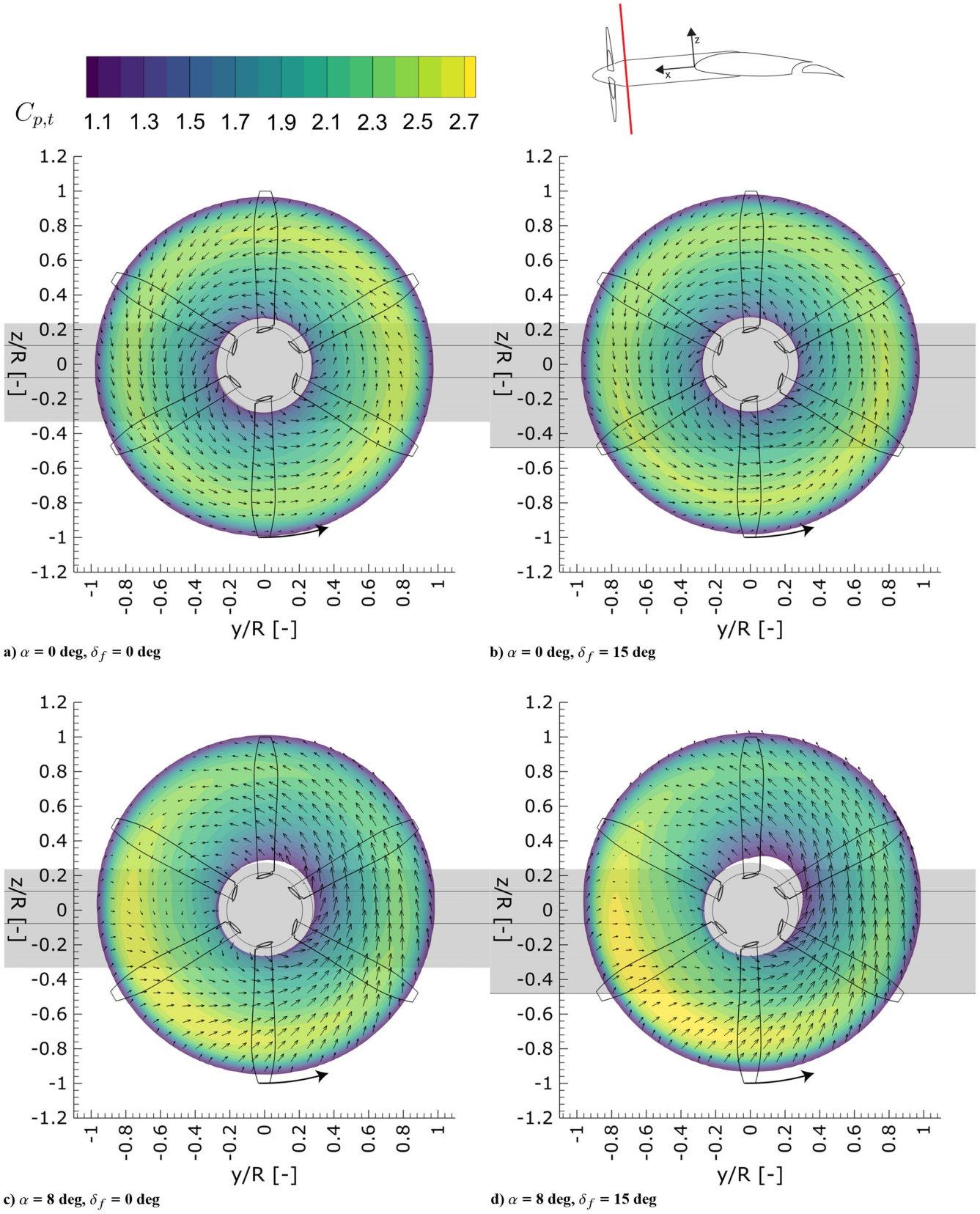

Fig. 10 Slipstream slices in yz-plane at $x/c = 0.5$ (propeller frame), showing in-plane velocity vectors and the distribution of $C_{P,t}$. Slice perpendicular to propeller axis.

van Arnhem [28]. The gaps in the contours near the nacelle (e.g., in Fig. 10d) are not local deformation but local pressure losses. These are the result of separation on the blade root due to the in-plane velocity component.

Despite the clearly demonstrated impact of the wing-induced upwash on the propeller inflow at $\alpha = 0$ deg and $\delta_f = 15$ deg, the in-plane velocity vectors in the $\alpha = 0$ deg configurations (Figs. 10a and 10b) are dominated by the swirl of the propeller. At higher angles of attack (Figs. 10c and 10d), the swirl is still clearly present but of the same order of magnitude as the vertical component of the freestream and the wing upwash. At the nacelle, this causes the flow on the downgoing blade side to flow against the

swirl direction. This has a significant impact on the development of a pair of vortices originating from the nacelle region and will be discussed further in Sec. III.D.

Close behind the propeller, the impact of the wing upwash and freestream incidence angle is mostly seen in the shifting of the disk loading and the local swirl. The same flow components convect the slipstream toward the wing upper surface as it moves closer to the wing. For configurations at low angles of attack (and low lift), this displacement is insignificant, but at higher angles of attack (and high lift), this causes significant slipstream deformation, as shown in Fig. 11. This occurs even before the slipstream interacts with the wing physically. We also see that the root losses on the upgoing

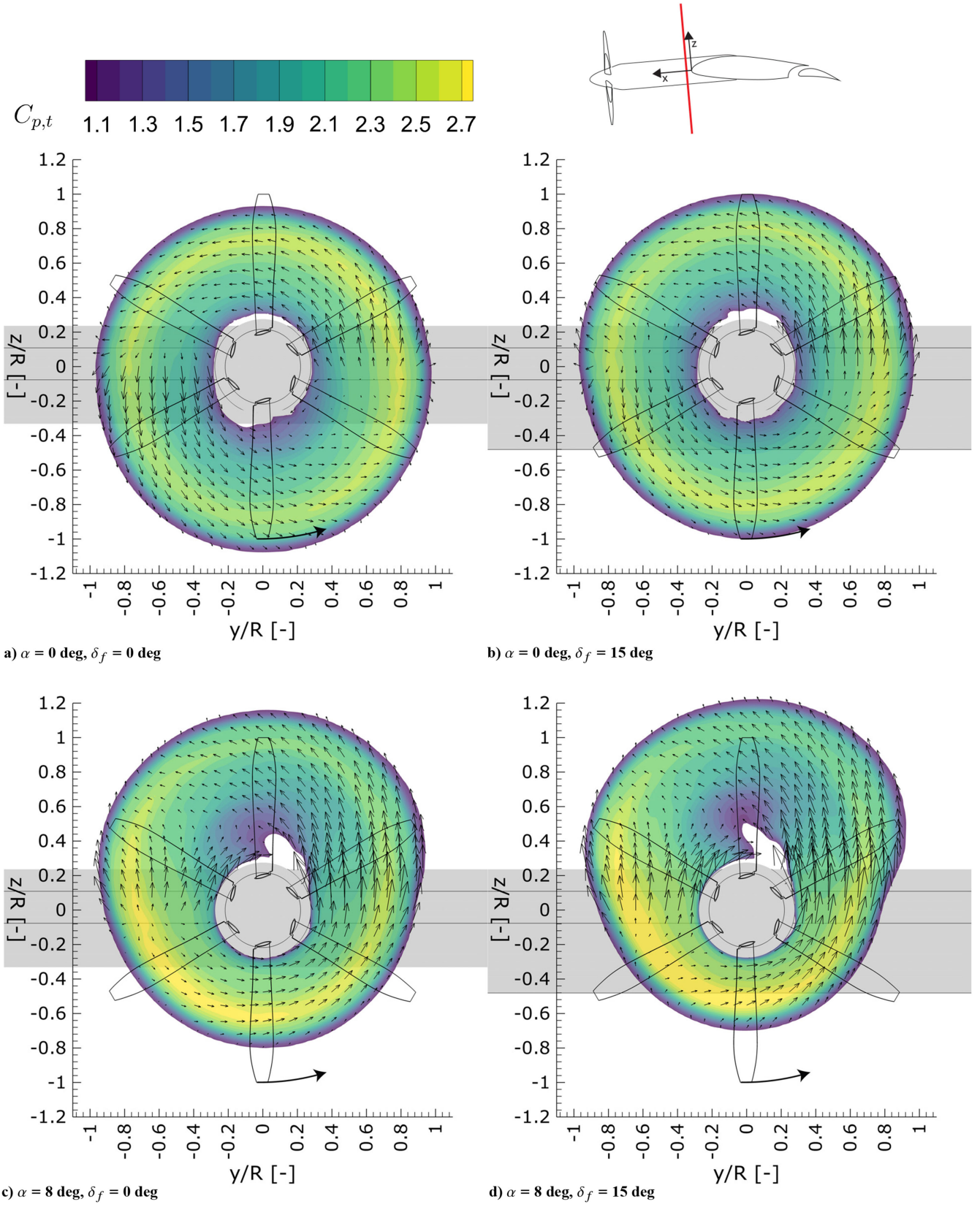

Fig. 11 Slipstream slices in yz-plane at $x/c = 0.02$ (just upstream of the leading edge), showing in-plane velocity vectors and the distribution of $C_{P,t}$. Slice perpendicular to propeller axis.

blade side convected toward the upper side of the nacelle, due to swirl and flow around the nacelle.

This deformation can be attributed to the region of flow acceleration around the wing leading edge. In that region, the slipstream is convected vertically much more than in the surrounding flow. The relative position of the slipstream with respect to the wing leading edge can then have a large impact on the slipstream deformation. Furthermore, the orientation and magnitude of the local velocity vectors at the wing leading edge can vary strongly between cases. For low α, the stagnation point of the wing is on the upper surface on the downgoing blade side, and the local velocity accelerates toward the lower surface. In the high α cases, the flow always accelerates from the lower to the upper surface, and the local velocity magnitude is much higher.

These effects are all highly dependent on the particular wing configuration. A different vertical installation position of the propeller, or a different distance between the propeller and the wing leading edge, will change how the slipstream will displace before it reaches the wing and therefore how it interacts with the wing itself. In literature on propeller–wing interaction, the importance of the horizontal propeller distance is often considered negligible with respect to the vertical position (e.g., Cui et al. [34]). Veldhuis [2] discusses the intersection of the wing with the velocity distribution in the slipstream. Clearly, in high-lift configurations these considerations change, as not only the loading distribution of the propeller and position of the slipstream are affected, but also its shape of the slipstream.

D. Region II: Over the Wing

At the start of region II, the slipstream physically interacts with the wing and splits into parts that move on both sides of the wing. We have already established that the vertical position of the slipstream just ahead of the wing leading edge is dependent on the freestream angle of incidence and the wing upwash. The impact of the vertical shifting position becomes evident from Fig. 12, showing slices of the slipstream at 5% chord downstream of the leading edge. Overall, the slipstream shape is still very close to that presented in Fig. 11. For the low α cases, the slipstream is split into two nearly equal portions. For higher α, the slipstream is positioned much higher with respect to the wing, and the majority of the slipstream moves along the wing's upper surface.

In addition to splitting the slipstream, the primary effect of the interaction at the leading edge (illustrated in Fig. 12) is the spanwise displacement of the slipstream near the wing surface. Felli [3] attributes this displacement of the slipstream edge (or more precisely, the tip vortices) to two main mechanisms: image vortex effects and pressure gradient effects. Regarding the image vortex effects, Felli [3] identifies two dominant contributions: the streamwise component of vorticity along the wing surface and the vertical component of vorticity at the wing leading edge, as illustrated in Fig. 13.

The initial spanwise expansion of the slipstream away from the propeller axis (hereafter referred to as the *outboard* direction) is primarily attributed by Felli [3] to the latter vortex image effect. However, he does not emphasize that the deformation of the tip vortices significantly influences the image vortex interaction. The outboard displacement is not confined to the tip vortices upstream of the leading edge but also affects the filaments wrapping around the leading edge itself.

The wrapping of the tip vortices around the wing leading edge, clearly shown by Felli [3] and in the λ_2 isosurfaces from our numerical simulations (Fig. 14), causes the entire vortex filament to experience self-induction in the outboard direction via image vortex effects. This is further illustrated in Fig. 15. Because these wrapped filaments lie very close to the wing surface, the induced image vortex effects are particularly significant. As the filaments extend further around the wing surface, they weaken, and consequently, the induced effect diminishes.

Furthermore, the interaction with the leading edge deforms the tip vortex structure near the wing, as again evidenced by the λ_2 isosurfaces in Fig. 14. In this near-surface region, most of the vorticity in the tip vortices on the upgoing blade side becomes reoriented upstream, opposite to the direction typically observed in undisturbed tip vortices. This is schematically depicted in Fig. 16. The upstream orientation alters the direction of self-induction due to the first image vortex mechanism (Fig. 13a), compared to the situation described by Felli [3].

At this stage, it is unclear whether the differences between our observations and those reported by Felli [3] or earlier works such as Felli and Falchi [18] and Muscari et al. [19] stem from variations in configuration or represent more general phenomena. The deformation of the tip vortex depends on the ratio between the vortex core size and the wing leading-edge radius [35–37], a parameter likely quite different in our configuration compared to the geometry used in the aforementioned studies.**

In addition to the image vortex effects, the slipstream edge is also displaced by the local spanwise pressure gradients [3]. For a symmetrical, nonlifting wing, we can identify three main contributions: scaling of the local pressure due to increased dynamic pressure in the slipstream, the angle of attack induced by the tangential velocities in the slipstream, and the local static pressure field behind the propeller. For a lifting wing, however, the pressure distribution around the wing changes compared to the nonlifting wing, both inside and outside the propeller slipstream. The various contributions of how the local static pressure is changed compared to the freestream pressure are illustrated in Fig. 17. Note that only the effect of tangential velocities is dependent on the rotation direction of the propeller. Additionally, note that the impact of angle of attack also changes the sign of the effect of dynamic pressure scaling. The direction of the induced crossflow due to the spanwise pressure gradients can thus completely change for a lifting wing, particularly in high-lift conditions.

It is worth noting that the vortex imaging effects and the pressure gradients are not fully decoupled features of the flow. Rather, the image vortex effects have a direct impact on the local pressure field. However, this impact is very small compared to the global effects of freestream, slipstream flow, and wing shape on the pressure field. We therefore treat the image vortex effects as independent of the pressure gradient effects.

The strength and direction of the spanwise pressure gradient effects are thus dependent on the relative balance between the contributions illustrated in Fig. 17 and will therefore differ with configuration and operating condition. Figure 18 shows the spanwise distribution of the static pressure coefficient C_p on the wing surface at $x/c = -0.05$ for two different configurations. The arrows indicate the direction of local convection imposed by the pressure gradient on the tip vortices. For $\alpha = 0$ deg and $\delta_f = 0$ deg (Figs. 18a and 18c), the pressure gradients emphasize the outboard displacement at the upper left and bottom right quadrants, while they oppose the image vortex effect on the upper right and bottom left quadrants. For $\alpha = 8$ deg and $\delta_f = 15$ deg (Figs. 18b and 18d), however, the pressure gradients cause outboard movement on the wing's lower surface and inboard movement on the wing upper surface.

Reviewing the slipstream shapes in Fig. 12, we clearly see the various contributions at play. In Fig. 12a, the most elongation is found at the upper left and lower right quadrants, where both vortex image effects and pressure gradient effects work in the same direction. The deformation at the lower left and upper right quadrants is smaller, as the pressure gradients oppose the image vortex effects. In Figs. 12c and 12d, the deformation on the wing's lower surface is much larger than on the wing upper surface, as the pressure gradients work in the same direction as the vortex image effects. Furthermore, the pressure gradients in the high α cases are much larger than in the low α cases, increasing their impact on the deformation.

Similar to the vortex imaging effects, the impact of the spanwise pressure gradients is concentrated near the wing surface and the leading edge. The pressure gradients are strongest close to the wing surface and diminish quickly when moving away from the surface, as shown in Fig. 19a. Similarly, the pressure gradients are strongest close

**All aforementioned studies on propeller–rudder interaction share the same geometry.

to the wing leading edge and diminish quickly further downstream (although they do not disappear completely), as shown in Fig. 19b.

The slipstream deforming much closer to the surface than away from it, at least initially when it physically interacts with the wing, also means that surface flow alone does not adequately represent the state of flow around the wing in propeller–wing(–flap) configurations. Not all portions of the wing where the surface is washed by the slipstream are equally immersed. Particularly on the wing's lower surface in the high α cases, the leading-edge deformation effects cause a significant expansion of the slipstream area on the wing surface, while the overall shape and distribution of the slipstream have not changed much. This means for certain regions on

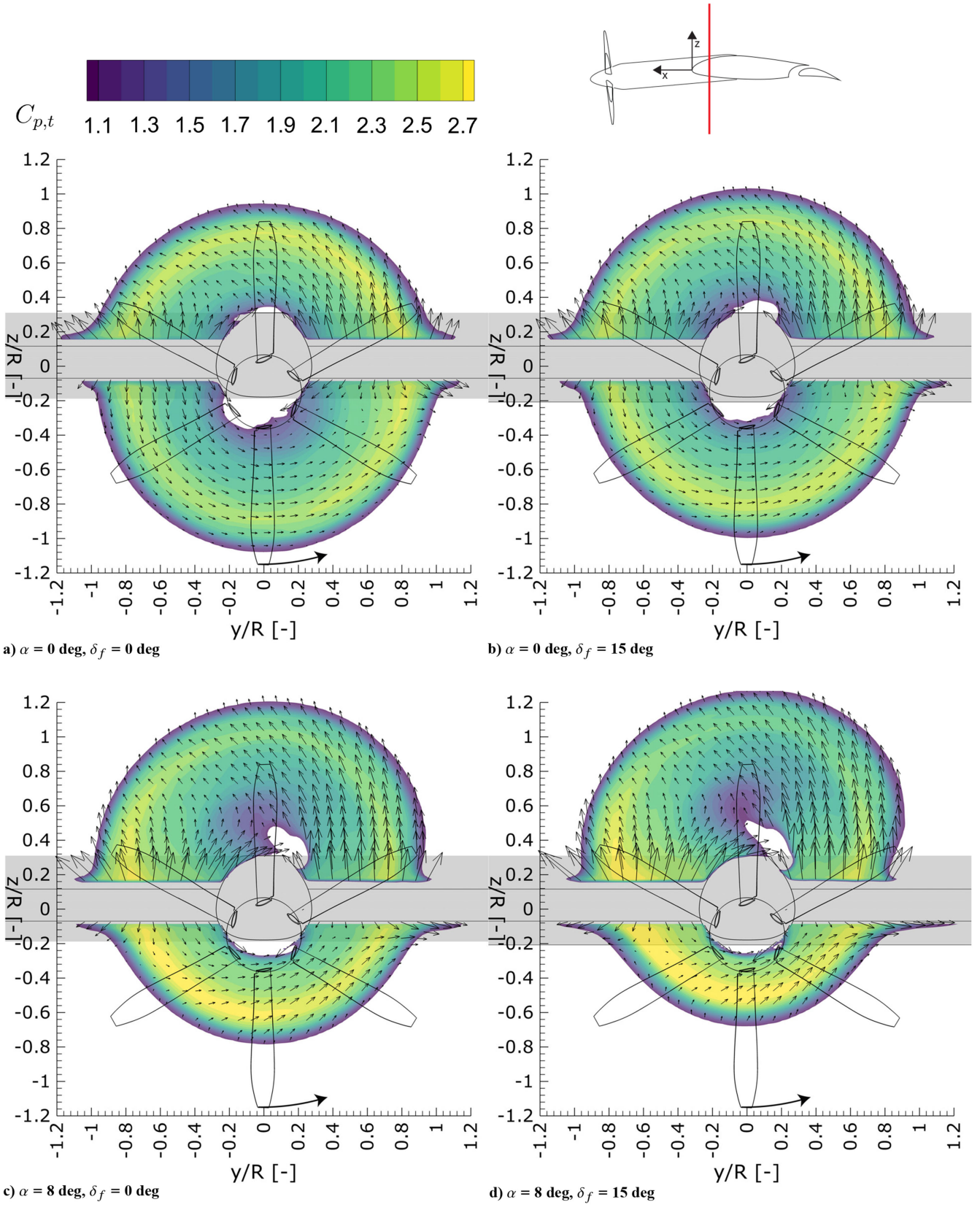

Fig. 12 Slipstream slices in yz-plane at $x/c = -0.05$ (just downstream of the leading edge), showing in-plane velocity vectors and the distribution of $C_{P,t}$. Slice perpendicular to flap nested wing chord.

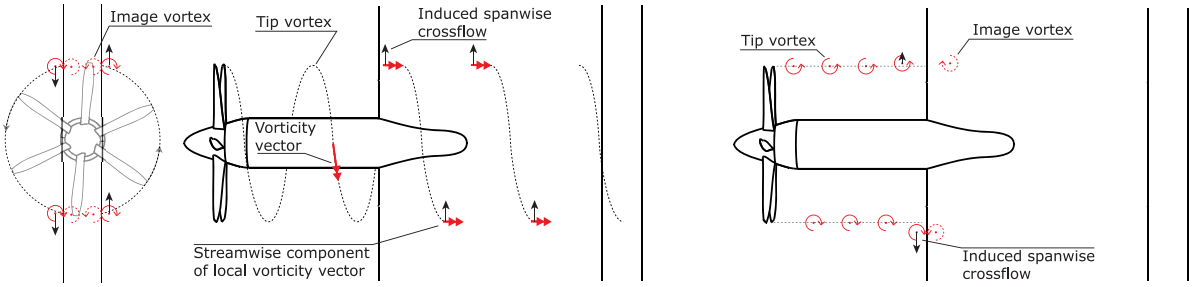

a) Imaging of the streamwise vorticity component in the wing surface

b) Imaging of the vertical vorticity components in the wing leading edge

Fig. 13 Schematic illustration of the image vortex effects of the slipstream vorticity in the wing leading edge and over the surface.

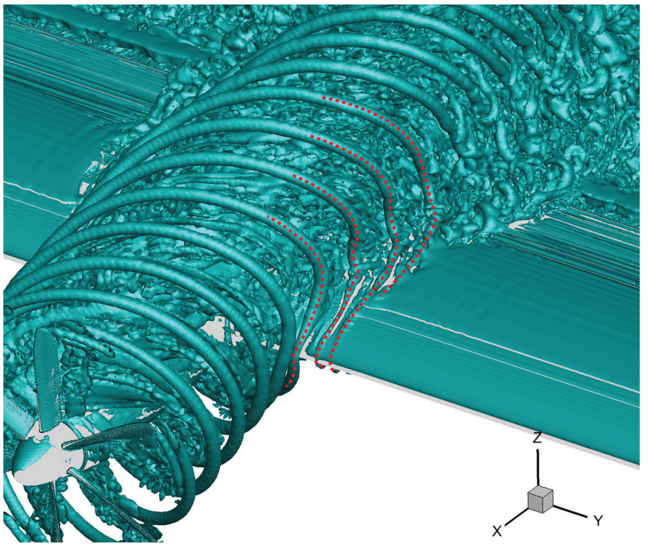

Fig. 14 Isosurfaces of $\lambda_2 = -5V_\infty^2/c^2$ showing the tip vortices wrapping around the leading edge and displacing outboard; $\alpha = 8$ deg, $\delta_f = 15$ deg.

the wing the boundary layer is affected by the slipstream, but shortly off the surface there is no slipstream and thus no rise in total pressure.

As the tip vortex elements that are wrapped around the leading edge displace, they pull and stretch parts of the slipstream that are further away from the wing surface. By the time the slipstream reaches the main element cove area, it has deviated significantly from its initial circular shape, as shown in Fig. 20. In particular, the edges of the slipstream that are close to the wing surface have expanded, and the gradients have diffused.

This expansion and diffusion is a result of interactions between the various tip vortex filaments that become aligned with the wing surface at the edge of the slipstream. Felli [3] showed that these filaments remain connected to the main tip vortex along the entire chord of the wing. Between these filaments, secondary vortices of opposite sign are induced in the wing boundary layer, as shown in Fig. 21. The secondary vortices wrap around the tip vortex filaments, as do the filaments themselves. The latter is visible more clearly in Fig. 21b. Overall, the slipstream boundary becomes diffused due to the various vortex–vortex and vortex–boundary-layer interactions, leading to a loss of the tip vortex helical structure.

The strength of the vortex that forms from the stretched tip vortex filaments at the slipstream edges varies depending on the alignment between the deformed tip vortex filaments and the orientation of the undisturbed helical vortex system of the slipstream. This mechanism is illustrated in Fig. 22.

On the upper surface downgoing blade side, the deformation of the tip vortex as it wraps around the wing leading edge reinforces the orientation of the original (undeformed) helical structure. As a result, a substantial portion of the tip vortex contributes to the formation of a strong vortex at the slipstream edge. In contrast, on the upper surface upgoing blade side, the deformation of the tip vortex opposes the natural orientation of the undeformed helical system. Consequently,

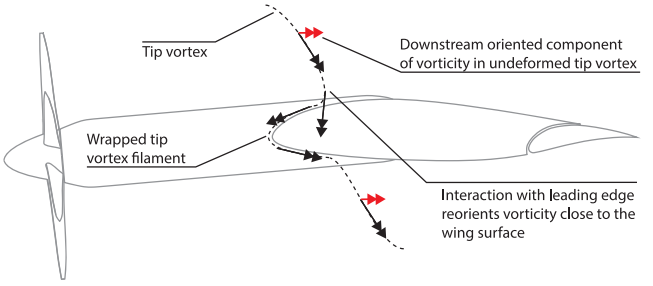

Fig. 16 Schematic illustration of the reorientation of vorticity in the tip vortices on the upgoing blade side due to the interaction with the wing leading edge.

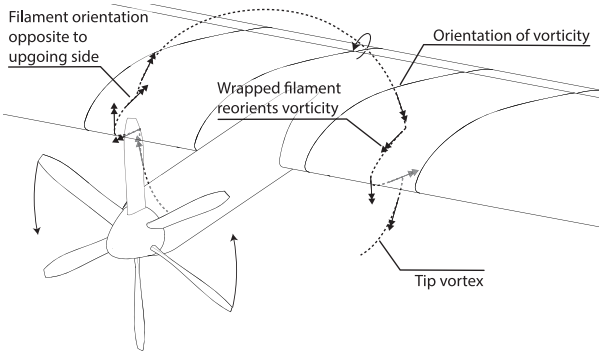

a) Orientation of tip vortices around the wing leading edge

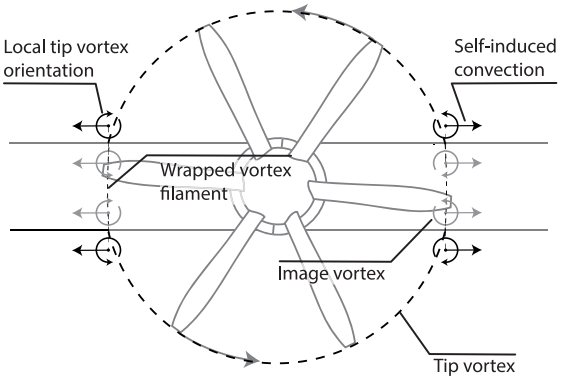

b) Vortex imaging effect of wrapped tip vortex filaments

Fig. 15 Schematic illustration of the tip vortex wrapping and imaging effect in the wing surface.

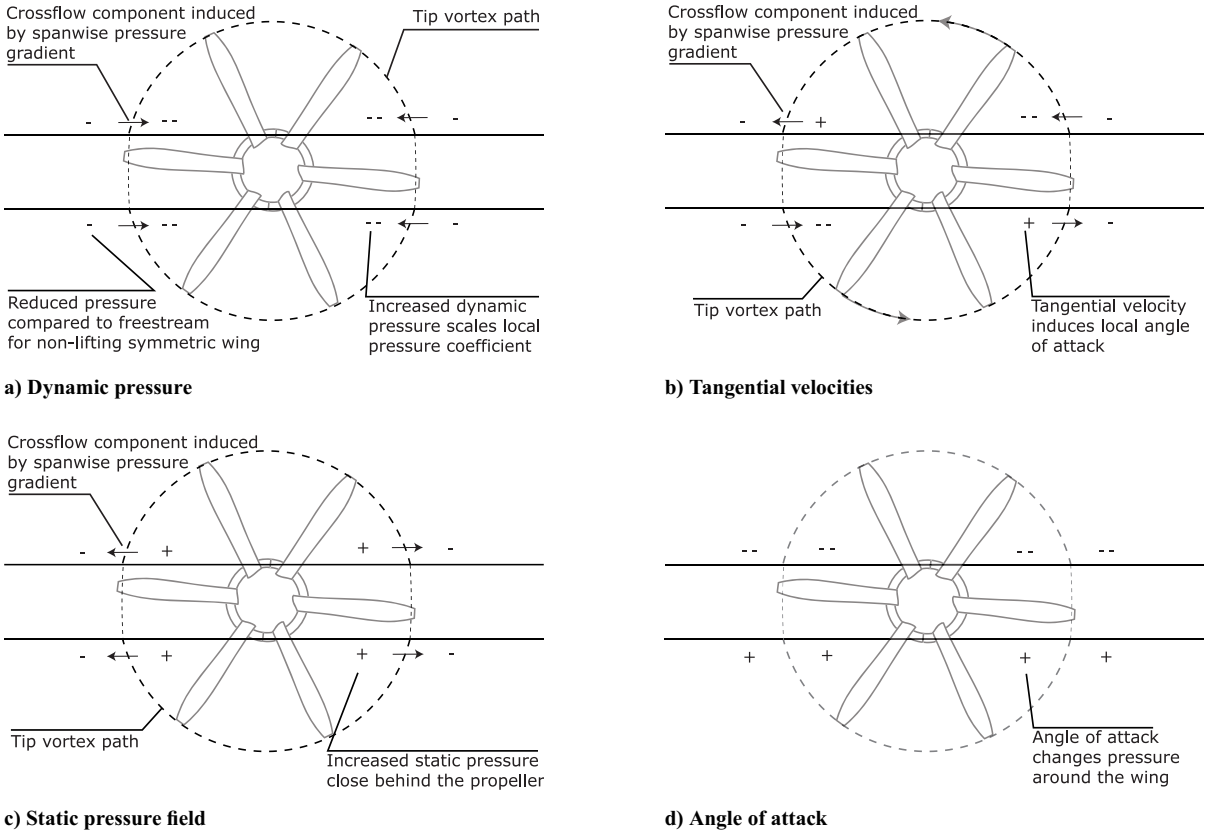

Fig. 17 Schematic illustration of the four main contributions to the spanwise pressure gradients induced by propeller–wing interaction on a lifting wing. Front view.

only the deformed filaments align along the wing surface, resulting in the formation of a much weaker vortex. A similar pattern is observed on the lower surface, mirrored across the center line.

This alignment mechanism is further influenced by the wing-induced circulation, which induces a rotation on the tip vortex helix. Figure 23 illustrates this effect on each side of the propeller. On the upgoing blade side, the tip vortices are rotated to become more perpendicular to the wing chord. On the downgoing blade side, they become more aligned (i.e., more parallel) with the chord. This rotation enhances the alignment between the vortex filaments and the wing surface on the downgoing side, increasing the portion of the tip vortex that participates in the surface interaction.

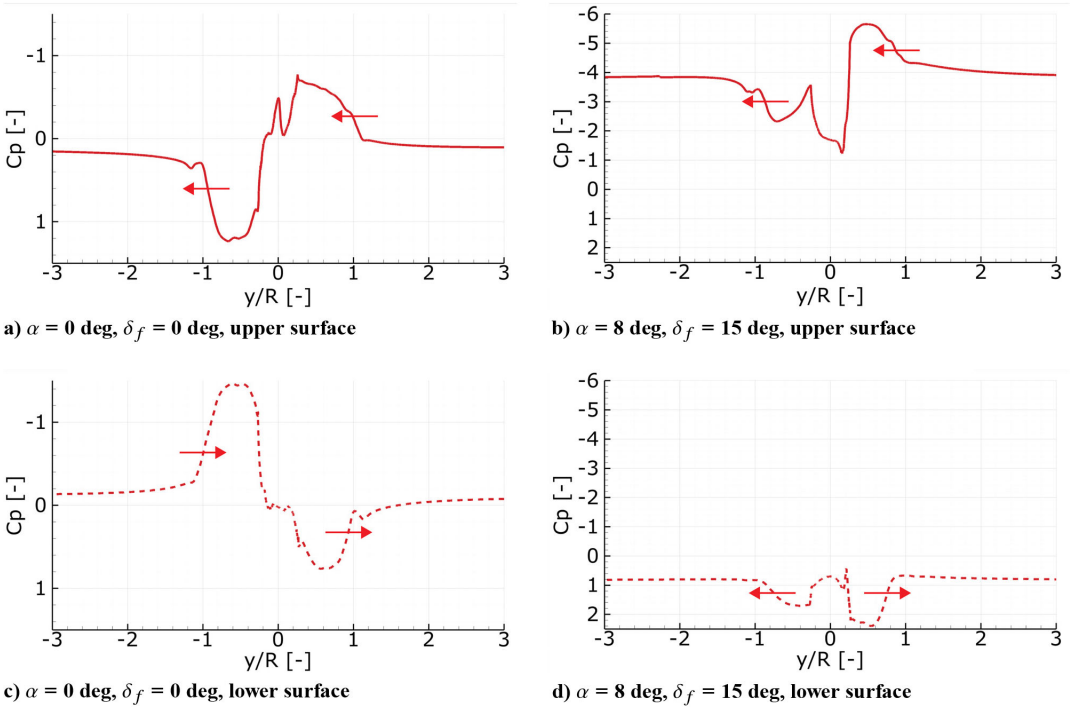

Fig. 18 Spanwise pressure distributions at $x/c = -0.02$ on the upper (solid) and lower (dashed) surfaces. Arrows indicate the direction of the crossflow component induced by the pressure gradient at the slipstream edge.

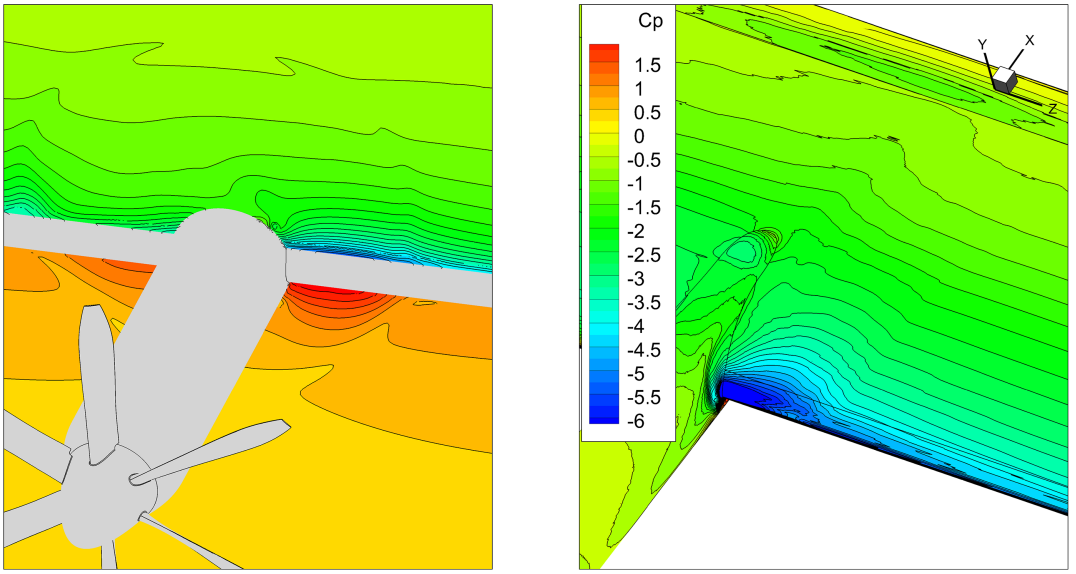

a) yz-slice at $x/c = -0.02$ **b) Surface**

Fig. 19 Contours of static pressure coefficient in a volume slice near the leading edge and on the wing surface; $\alpha = 8$ deg, $\delta_f = 15$ deg.

At higher angles of attack, asymmetric disk loading further amplifies this effect. The tip vortex strength increases on the downgoing blade side, reinforcing the vortex roll-up and resulting in a significantly stronger surface-bound vortex on that side.

These observations yield several valuable insights to be investigated further. The relation between deformation and helix angle suggests that deformation may be mitigated to a degree by designing for lower advance ratios. This may prove particularly interesting for distributed propeller cases, where deformation will increase interactions between adjacent slipstreams.

From the slices of $C_{p,t}$ in Fig. 20, we can also identify a concentrated region of total pressure loss at the center of the slipstream. This is the viscous core of a vortex that rolls up at the nacelle on both sides of the wing. Figure 24 visualizes these *nacelle-root vortices* by isosurfaces of the x-component of vorticity (in wing frame). Vorticity distributed around the nacelle body rolls into a pair of concentrated vortices near the wing leading edge. These vortices are hereinafter referred to as the *nacelle/root vortices*, since they consist of vorticity on the nacelle surface and the propeller blade root vorticity. For low angles of attack, these vortices are of comparable strength on both sides of the wing and reach far into the wake region. For higher angles of attack, the vortex on the upper side is much stronger. We can still see a vortex on the lower side, but this breaks down before it reaches the cove. The residual momentum loss from the vortex core of this vortex later impinges on the flap.

The formation of the nacelle/root vortices is based on vortex convection and stretching, similar to the tip vortices wrapping around the leading edge. The sources of vorticity for the formation of the nacelle/root vortex are the vorticity in the nacelle boundary layer and the propeller blade root vortex. The former will be relatively small compared to the latter, particularly at low angles of attack. The propeller root vorticity can be decomposed into longitudinal (or streamwise) and azimuthally oriented vorticity, as is common in slipstream tube models. Figure 25 illustrates how these two parts of the vortex system will interact with the wing leading edge to form the nacelle/root vortex. The vortex lines are all positively oriented and will wrap into a concentrated vortex when they are convected into each other by flow around the nacelle and wing leading edge. The vortex rings will fold around the nacelle and wing leading edge, reorienting into a vortex pair on each side of the wing. The positive-oriented part of the deformed vortex rings will wrap into the same vortex as the deformed vortex lines, leaving the negative-oriented part of the deformed vortex rings to form a much weaker, negative-oriented nacelle/root vortex. The illustrations of Fig. 25 thus predict a vortex pair on each side of the wing, with the positive-oriented vortex stronger than the negative-oriented vortex. This vortex pair will self-induce a velocity component away from the surface of the wing. Furthermore, the vortex on the upper surface will be stronger than on the lower surface, particularly for high-lift conditions.

The mechanism illustrated in Fig. 25 is supported by looking at slices of vorticity along the nacelle and wing. Figure 26a shows the component of vorticity aligned with the wing chord, which roughly equates to the local flow direction. Along the nacelle, the vorticity is mostly evenly distributed and fully positive. As we get closer to the leading edge, we can see the orientation flip. The upper right and lower left quadrants become negative as the root vorticity wraps around the leading edge. Further downstream on the wing we see a distinct vortex pair. The negative-oriented vortex is weaker and dissipates, leaving only the positive vortex to move further down the wing.

For higher angles of attack, the described mechanism no longer seems to hold, as shown in Fig. 26b. However, when visualizing the vortex structures in the time-accurate results (Fig. 27), they can in fact still be observed. Because the angular velocity of the blade is much lower at the root than at the tip, the root vorticity is already strongly aligned with the flow. This causes a large portion of the root vortices to directly roll into the nacelle/root vortex. Residual root vortices still wrap around the leading edge, and a small portion rolls into the nacelle/root vortex on the wing's lower surface. Additionally, due to the positive angle of incidence of the nacelle, local flow around the nacelle also induces vorticity in the nacelle boundary layer. On the downgoing blade side, this opposes the root vorticity.

Revisiting Fig. 20, we can see that the nacelle vortices dominate the in-plane velocities near the wing surface downstream of the nacelle, inducing a strong spanwise velocity component on the wing surface. The latter drives flow from the downgoing blade side into the upgoing blade side, creating a shear layer at their interface. This shear layer is illustrated in Fig. 28 by slices of $C_{p,t} < 1$. From oil flow visualization (see Fig. 29), we have seen this shear layer causing local flow separation and confluencing with separation regions outside the slipstream at very high angles of attack. The effects of the nacelle/root vortex may thus limit the wing performance in the maximum lift regime.

A different position of the nacelle could greatly change the interaction of the nacelle/root vortex with the wing surface flow. A nacelle under the wing, for instance, would mean all the root vorticity convects along the lower surface. This would mitigate the crossflows on the upper surface and thus the shear layer shown in Fig. 28 and associated flow separation. However, such a nacelle

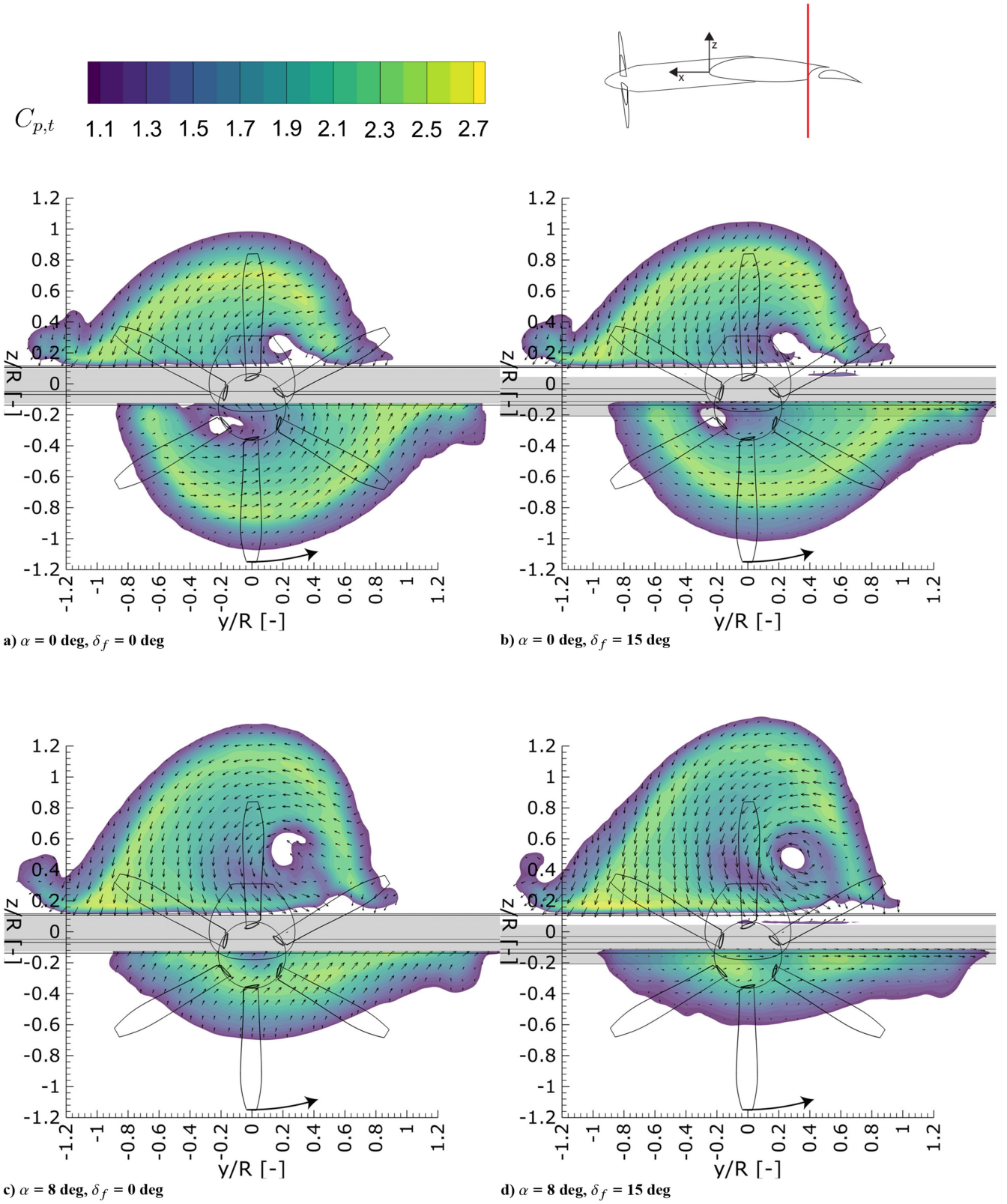

Fig. 20 Slipstream slices in yz-plane at $x/c = -0.67$ (at the main element cove), showing in-plane velocity vectors and the distribution of $C_{P,t}$. Slice perpendicular to flap nested wing chord.

position would also result in more of the nacelle vorticity impinging on the flap, which may affect it negatively. Furthermore, the nacelle position has a direct impact on the propeller–wing interaction, depending on the propeller diameter. Nonetheless, the role of the nacelle/root vortex in the wing surface flow development further emphasizes that the nacelle integration is a critical aspect of propeller–wing interaction, particularly in high-lift conditions.

Overall, the slipstream deformation on the main element is evidently dominated by the tip and root vortices wrapping around the leading edge. The resulting nacelle/root vortex dominates the flow phenomena that occur within the boundaries of the slipstream, while the deformation of the slipstream boundaries is determined by the tip vortex filaments that align and gather at the slipstream edges.

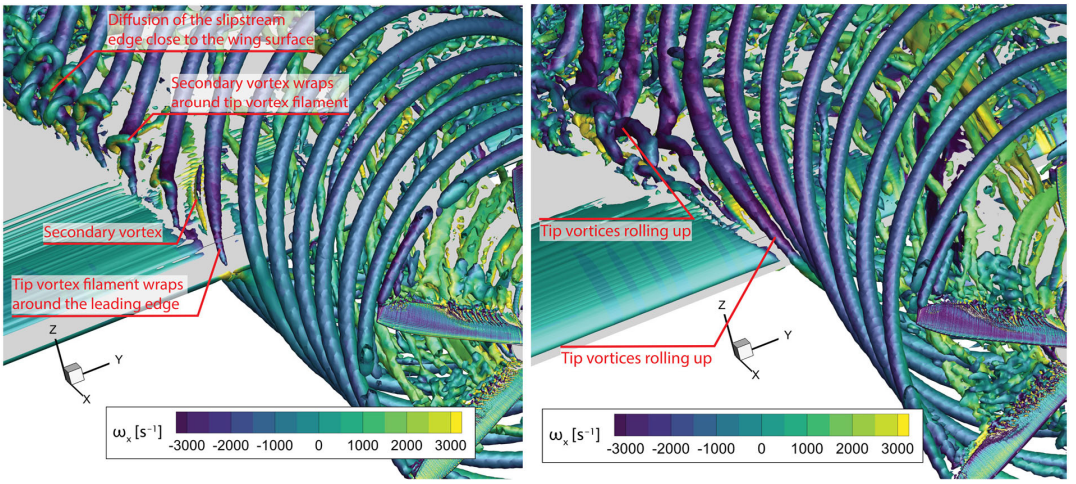

a) $\alpha = 0$ deg, $\delta_f = 0$ deg **b)** $\alpha = 8$ deg, $\delta_f = 15$ deg

Fig. 21 Isosurfaces of $\lambda_2 = -100V_\infty^2/c^2$, showing the alignment and roll-up of the stretched tip vortex filaments on the wing surface. Colored by vorticity component parallel to the wing chord.

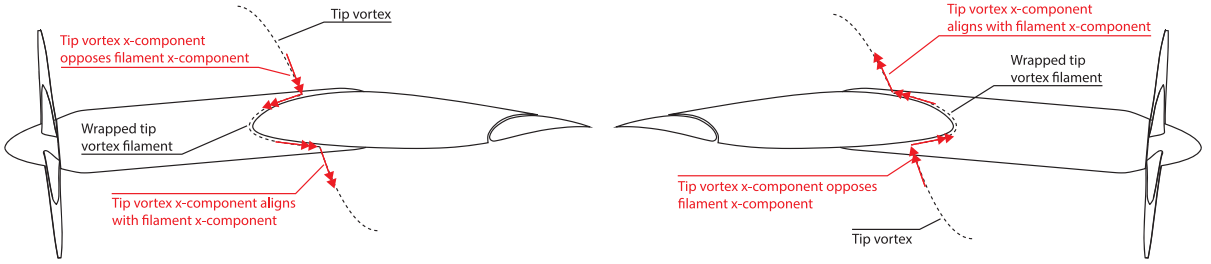

a) Upgoing blade side **b) Downgoing blade side**

Fig. 22 Illustration of the alignment of the slipstream helix angle with the local deformation of the tip vortices, contributing to the vortex roll-up at the slipstream edge on the wing surface.

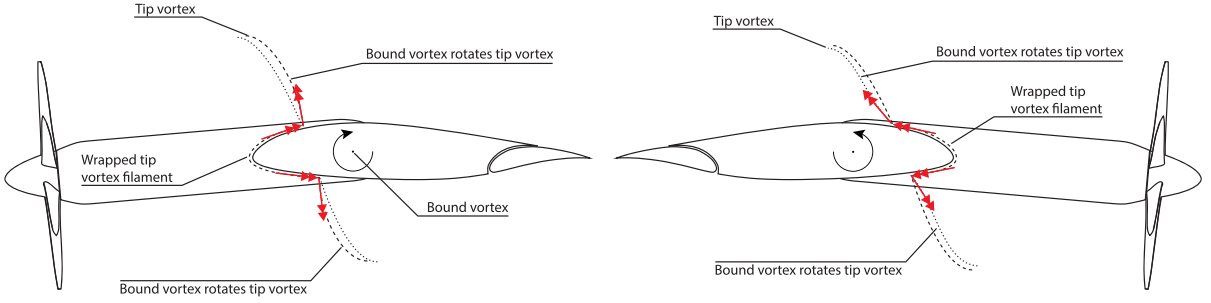

a) Upgoing blade side **b) Downgoing blade side**

Fig. 23 Illustration of the bound circulation of the wing rotating the slipstream helix, affecting the alignment of tip vortices that roll up near the wing surface.

The interaction of the slipstream with the flap differs significantly from the main element interactions. The flap has no nacelle, and root vorticity has readily formed into concentrated vortices aligned with the flow [4,25]. Furthermore, the flap is immersed in the part of the slipstream that travels along the wing's lower surface. Only a small portion of the flow moves through the gap, and, due to the deformation, no concentrated tip vortices wrap around the flap.

The rotation of the helical vortex system due to the wing circulation (see Fig. 23), as well as the pressure field around the flap, affects the spacing of the tip vortices on both sides of the wing. On the wing's upper surface, they are spaced further apart, delaying vortex–vortex interactions and breakdown of the helical vortex system. On the wing's lower surface, however, it is the opposite. The tip vortices are pushed into each other, forcing them to interact. This causes them to leapfrog and combine into larger vortical structures that eventually break down, as visualized in Fig. 30. The figure shows that this process, which we will denote as *vortex system instability*, occurs much earlier along the wing chord for configurations with stronger bound circulation.

Resulting from this interaction, the flow that immerses the flap is fairly uniform in the high-lift cases. As illustrated by the in-plane velocity vectors in Fig. 20, the high-lift cases show little asymmetry due to swirl effects. For lower lift cases, the swirl—and nacelle/root vortex effects—is still dominant. Overall, the flap lift is augmented due to the increase in dynamic pressure, and the resulting lift distribution is relatively symmetrical, as discussed previously in Sec. III.A.

Over the flap itself, the majority of deformation occurs on the upgoing blade side. Figure 31 shows the slipstream shape at the flap trailing edge. For clarity, the slipstream shape at the main element cove (Fig. 20) is shown using a single contour line of $C_{p,t} = 1.05$. Note that at the flap trailing edge, the upper half of the slipstream no longer interacts physically with any surface, as it has left the main

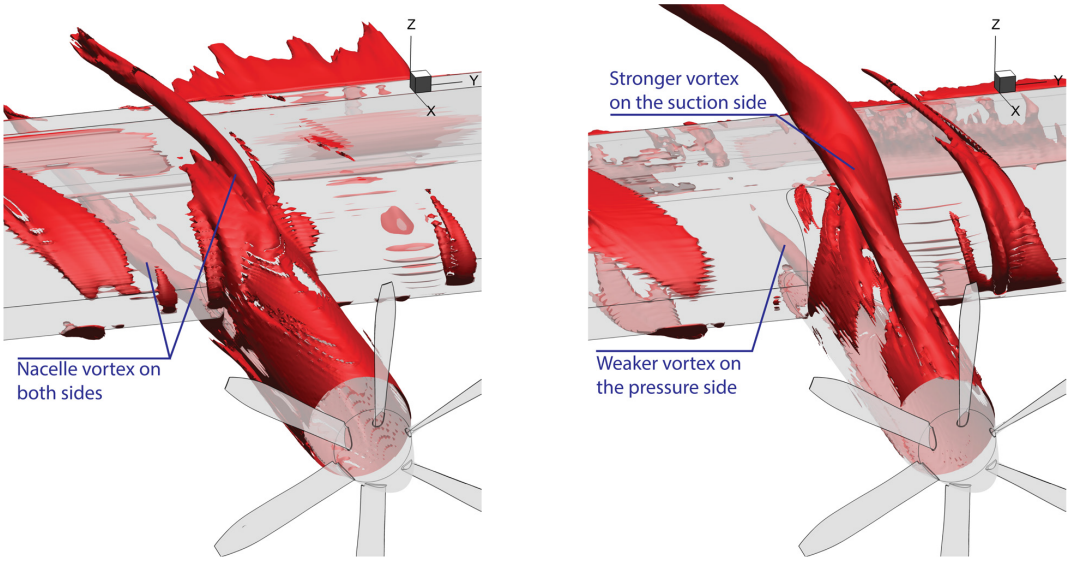

a) $\alpha = 0$ **deg,** $\delta_f = 0$ **deg** **b)** $\alpha = 8$ **deg,** $\delta_f = 15$ **deg**

Fig. 24 Isosurface of the *x*-component of vorticity (in wing frame) at $\omega = -3000$ s^{-1}, showing the formation of a vortex on both sides of the wing from vorticity around the nacelle.

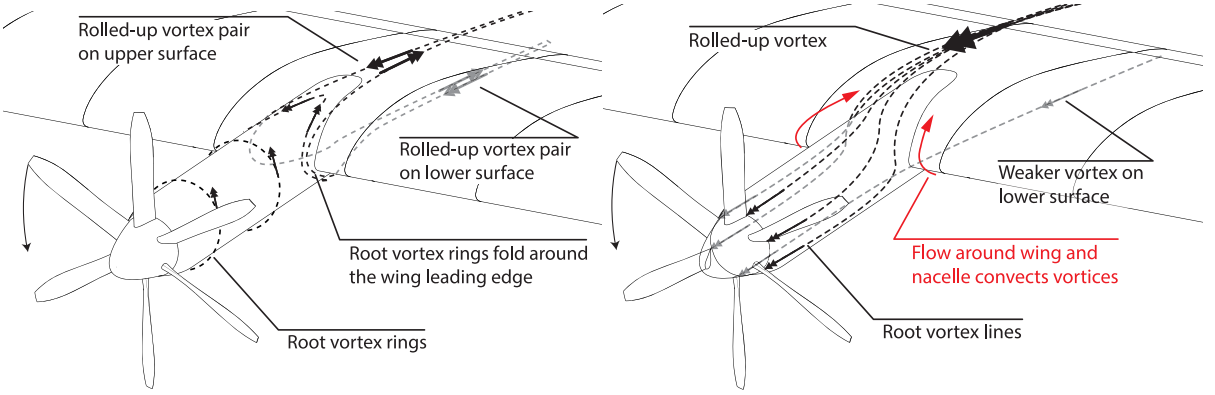

a) Root vortex rings **b) Root vortex lines**

Fig. 25 Illustration of the root vorticity rolling up into the nacelle vortex at the wing leading edge, based on vortex ring and vortex lines decomposition.

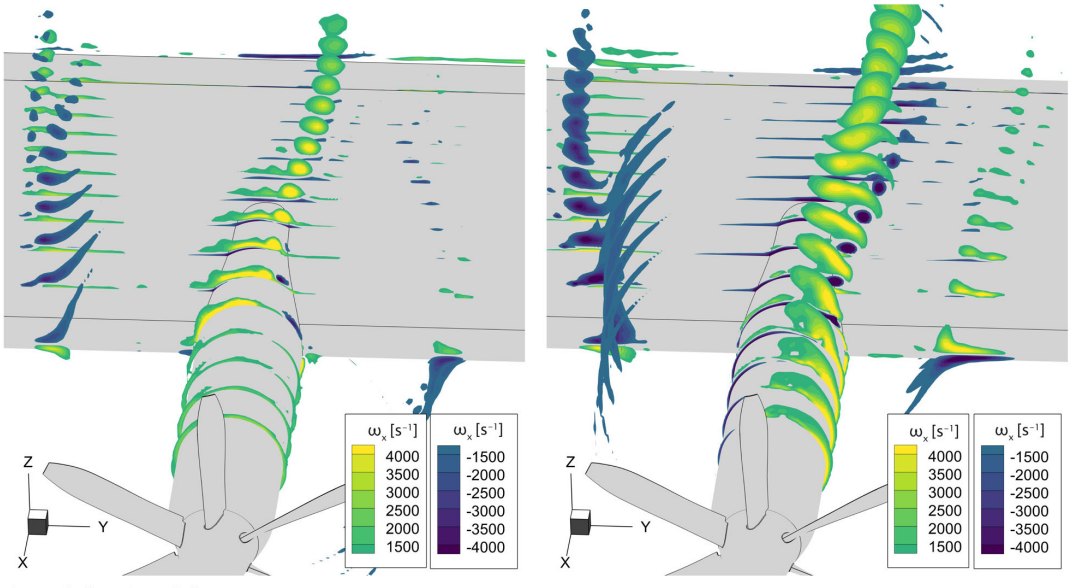

a) $\alpha = 0$ **deg,** $\delta_f = 0$ **deg** **b)** $\alpha = 8$ **deg,** $\delta_f = 15$ **deg**

Fig. 26 Slices of the *x*-component of vorticity (in wing frame) where $|\omega| > 1500$ s^{-1}.

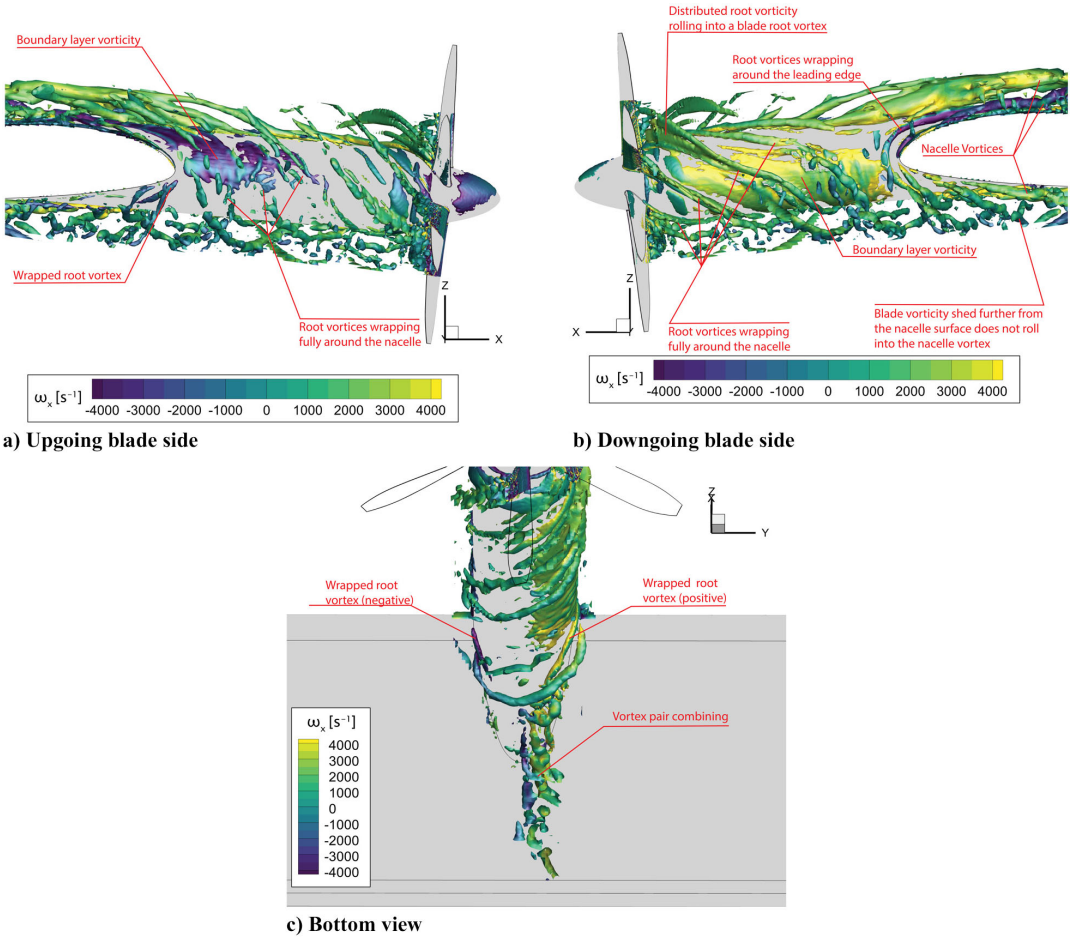

Fig. 27 Isosurfaces of $\lambda_2 = -10V_\infty^2/c^2$, showing the root vorticity roll-up around the nacelle. Tip vortex values were blanked to reveal the nacelle flow. Isosurface colored by the x-component of vorticity in the wing frame.

element and is separated from the flap element by the gap flow. The lower part of the slipstream impinges upon the flap surface, causing some spanwise expansion. Since it has been established that the slipstream no longer consists of a concentrated helical vortex system when it reaches the flap, no distinct vortices wrap around its leading edge, and no dominant vortex imaging effects take place. The deformation of the slipstream on the flap will then be dominated by the pressure gradient effects.

E. Region III: Wing Wake

The final stage of deformation occurs in the wake of the wing, after the slipstream has left the flap trailing edge. Figure 32 shows the slipstream distribution and in-plane velocity vectors in the wake of the wing, at $x/c = -2$. At this stage, the slipstream has combined into a single structure again, although the two halves of the slipstream can still be clearly identified for the configurations at $\alpha = 0$ deg. The slipstream has clearly dissipated significantly compared to the flap trailing edge position (Fig. 31), owing to the breakdown of the vortex system and mixing with the wing and flap wakes. It should be noted that at this point, numerical dissipation and diffusion in the simulations will also have a significant impact on the distributions.

Regardless of the contribution of numerical dissipation to the gradients of the slipstream distribution in the wake, we can see that significant deformation and redistribution occur after the slipstream leaves the wing trailing edge. The in-plane velocity vectors are dominated by the (remainders of the) nacelle/root vortex, particularly for the high-α configurations. For configurations with flaps deployed, the lower right quadrant is dominated by the downwash rather than the nacelle/root vortex. Overall, this causes the slip-

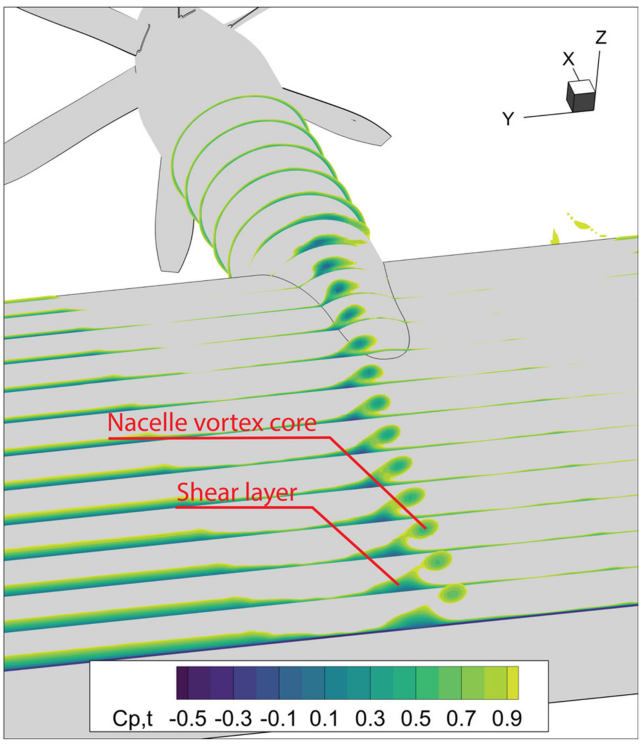

Fig. 28 Slices of total pressure coefficient $C_{p,t} < 1$, showing the shear layer due to the vortex-induced crossflow.

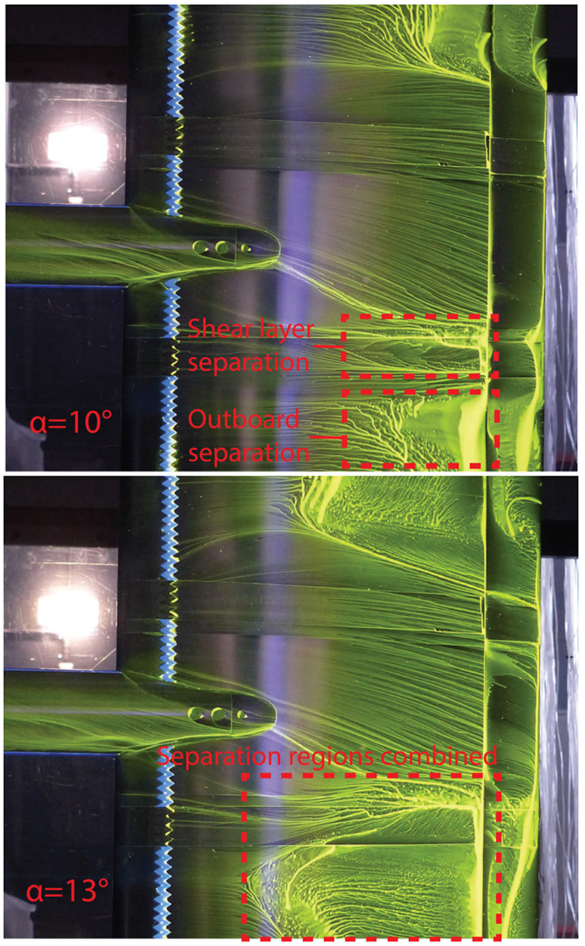

Fig. 29 Oil flow image showing flow separation resulting from the shear layer confluencing with the outboard separation; $\delta_f = 0$ deg.

stream to rotate around the nacelle/root vortex and continue to stretch toward the upgoing blade side.

These observations have two major implications. Firstly, the state of the slipstream in the wake of the wing cannot be used in a straightforward manner to judge the deformation of the slipstream on the wing. Despite the significant deformation that takes place on the wing up to the flap trailing edge, the slipstream maintains much more of its circular shape than the wake images would lead us to believe. Particularly the extent of shearing of the slipstream on the wing may be overestimated from the wake measurements alone.

Secondly, the deformation of the slipstream in the wake may be critical to the aerodynamic performance of the empennage and flight stability in typical tube-and-wing aircraft configurations. Slipstream effects on the empennage are generally modeled using straightforward slipstream tube models (e.g., the method proposed by Obert [38], recently applied by Bouquet and Vos [39]). While this may prove sufficient in low-lift conditions to a certain degree, it is clear from the distributions shown in Fig. 32 that this assumption will not hold for high-lift configurations, particularly when flaps are deployed. Considering the deformation that takes place in the wake within a single chord distance, the impact of the slipstream on the empennage (or any other downstream surface) cannot be predicted accurately with standard slipstream modeling methods.

IV. Conclusions

In this paper, we have characterized the slipstream deformation due to propeller–wing aerodynamic interaction of an aeronautical propeller–wing–flap configuration at various angles of attack and flap deflections, based on validated numerical simulations. Overall, the slipstream deformation is dominated by effects of the physical interaction of blade tip and root vorticity with the wing surface. This causes spanwise displacement, vortex system instabilities, and vortex–boundary-layer interactions, leading to the overall deformation and diffusion of the slipstream.

We discussed different mechanisms of slipstream deformation based on three regions of the flow: between the propeller and wing, over the wing, and in the wake of the wing. Upstream of the wing,

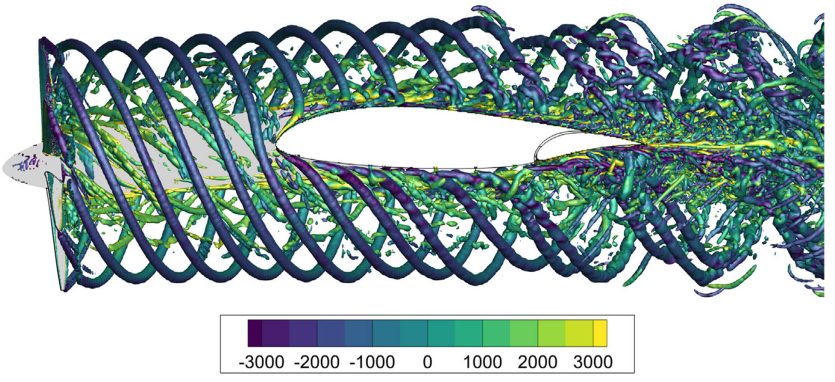

a) $\alpha = 0$ deg, $\delta_f = 0$ deg

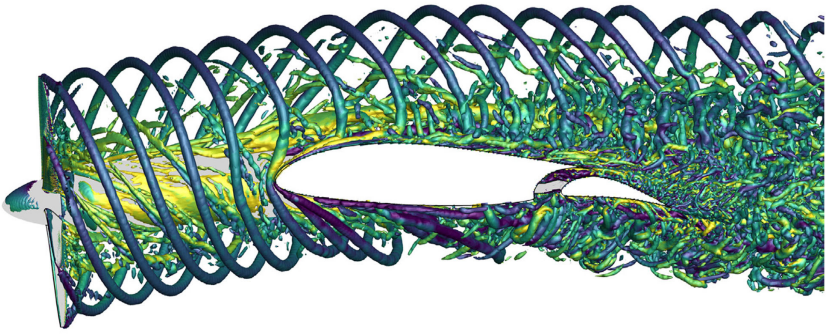

b) $\alpha = 8$ deg, $\delta_f = 15$ deg

Fig. 30 Isosurfaces of $\lambda_2 = -100V_\infty^2/c^2$, showing the breakdown of the helical tip vortex structure for different configurations. Colored by x-component of vorticity.

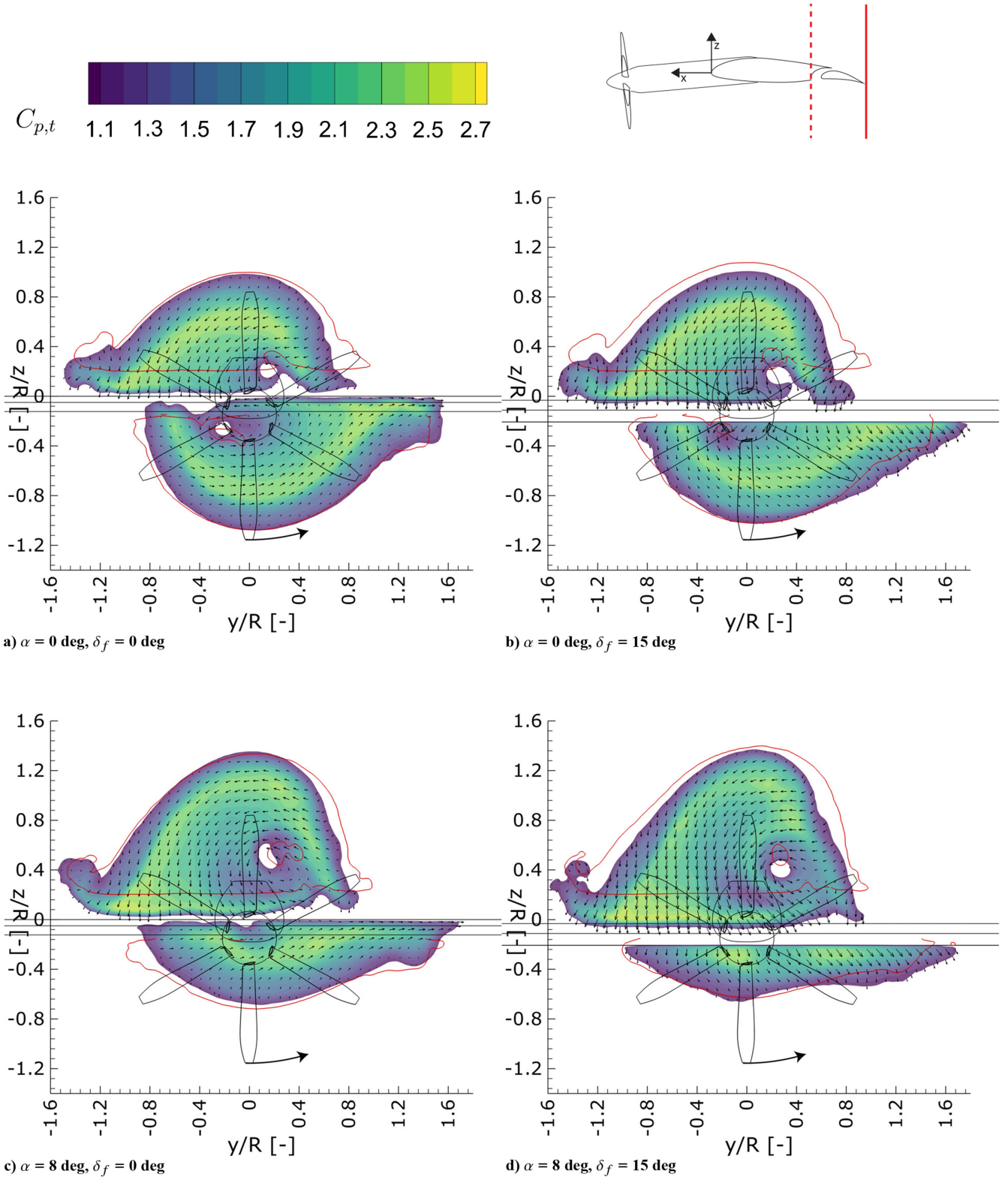

Fig. 31 Slipstream slices of velocity vectors and $C_{P,t}$ in yz-plane at the flap trailing edge. Red contour lines indicate slipstream shape at the cove for comparison.

significant deformation of the slipstream takes place depending on the position of intersection with the wing. This deformation is a result of vertical transport of the slipstream due to the local flow angle, as well as the interaction with the flow acceleration around the wing leading edge. When the intersection position is close to the center of the slipstream, the tip vortices are in line with the local flow acceleration, and their convection does little to deform the slipstream. At lower intersection positions, the tip vortices are at an angle to the local flow acceleration, resulting in a deformation of the circular slipstream shape.

As the slipstream physically impinges on the wing, the tip and root vortex systems are stretched around the wing leading edge. The root vorticity rolls into two vortex systems, one on each side of the wing. For higher wing circulation, more vorticity is convected to the upper surface of the wing, and the vortex on that side grows stronger. The tip vortices transport outward strongly at the wing

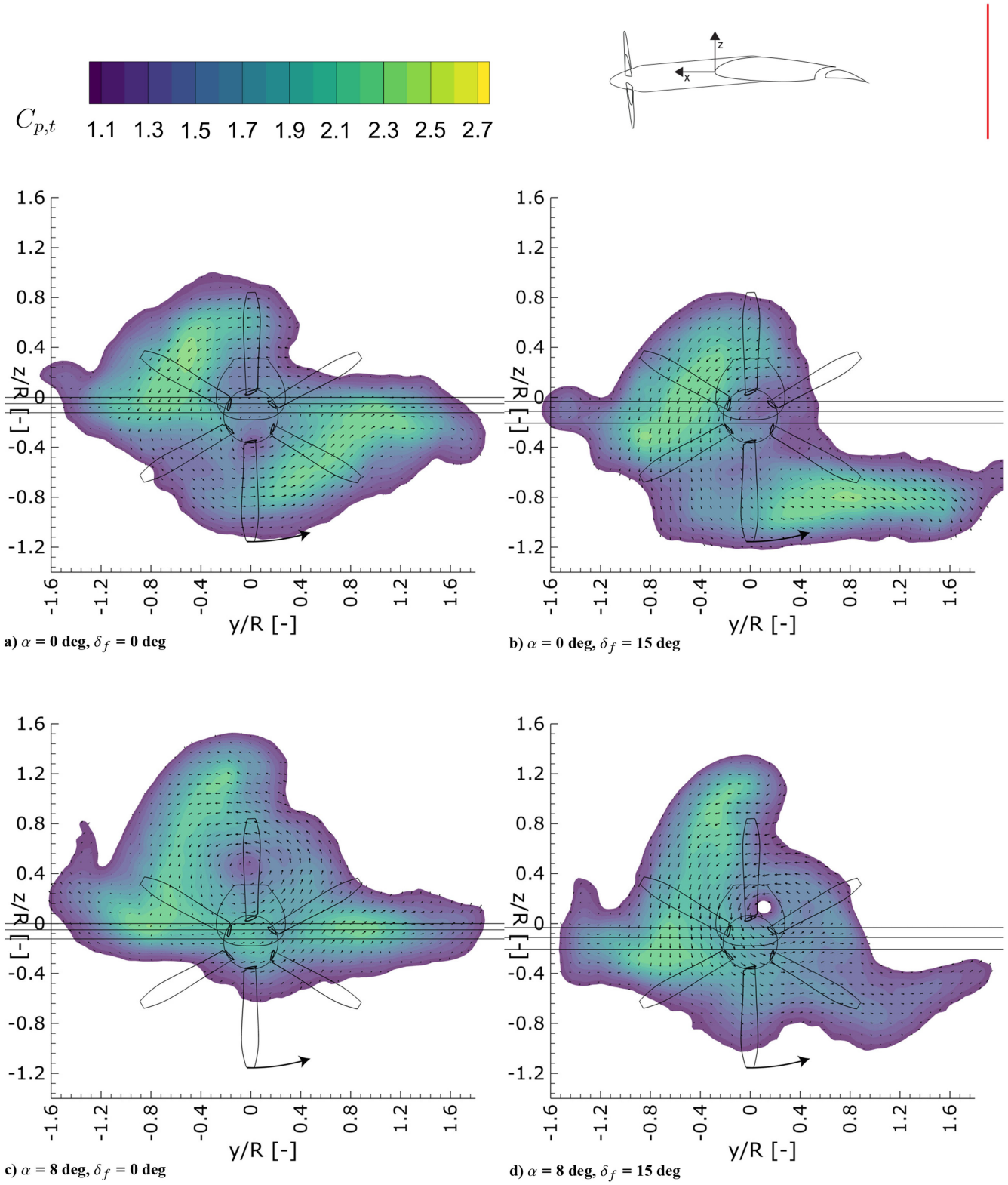

Fig. 32 Slipstream slices in yz-plane at $x/c = -2$ (in the wake), showing in-plane velocity vectors and the distribution of $C_{P,t}$. Slice perpendicular to flap nested wing chord.

leading edge, after which they align and roll into larger vortex systems at the slipstream edge. This effect is strongest on the downgoing blade side upper surface, where the tip vortices are already aligned more with the wing surface, further aided by wing circulation effects.

The rolled-up root vortex induces a strong crossflow component on the wing surface within the boundaries of the slipstream. This crossflow drives flow from the downgoing blade side into the upgoing blade side. At the interface, a shear layer develops that can locally separate at high angles of attack, possibly interacting with other local separation regions and limiting maximum lift.

The interaction of the slipstream with the flap differs significantly from the main element interactions. The flap is immersed in the part of the slipstream that travels along the wing's lower surface, and only a small portion moves through the flap gap. Unlike the main element, no concentrated vortices wrap around the flap leading edge. The interaction with the wing upstream of the flap affects the stability of the helical vortex system. Tip vortices are pushed into

each other on the lower surface, causing them to leapfrog and combine into a larger vortical structure. As a result, the flow affecting the flap is uniform and lacks swirl and thus does not impose asymmetrical loading such as is experienced by the main element.

Downstream of the wing, the deformation is dominated by the nacelle-root vortex, which imposes a dominant rotational component on the slipstream. Significant deformation takes place in the wake. At the flap trailing edge, the part of the slipstream that passes the upper surface of the wing still holds much more resemblance to its circular shape. This means immersion of the wing is not well represented by the slipstream shape in the wake. Additionally, the slipstream deformation clearly cannot be overlooked in the aerodynamic performance of downstream surfaces, such as the empennage. Particularly when flaps are deployed, the slipstream that reaches these downstream stations will not resemble a typical slipstream tube whatsoever.

The effect of the slipstream deformation on the lift distribution is significant, particularly for the flap. While the main element mainly experiences augmentation of the lift distribution within the area directly behind the propeller, the part of the flap that experiences lift augmentation due to the slipstream interaction is off-center and wider than a propeller diameter. Furthermore, it lacks the characteristic asymmetry imposed by swirl that is observed on the main element. This poses restrictions on which slipstream models are accurate for use in simulating propeller–wing–flap interactions.

The slipstream deformation discussed in this paper is specific to the tested geometry. Changes in, for instance, nacelle placement and integration will change the resulting slipstream shape. Nevertheless, the authors believe that most of the mechanisms described in this paper hold true for different geometries, as they depend on physical vortex deformations and interactions. The descriptions and visualizations of these mechanisms will aid researchers in understanding and predicting the deformation in different configurations as well.

The discussion in this paper reveals several phenomena that would be of interest to future research. The aforementioned sensitivity to the considered geometry should be explored further, particularly the impact of nacelle placement and how it may be used to mitigate detrimental effects of the aerodynamic interaction near maximum lift. Additionally, the hypothesis that slipstream deformation may be mitigated by designing for lower advance ratios, thereby increasing the tip vortex helix angle with the wing chord, is worth exploring further, particularly in the context of distributed propulsion. In general, the impact of additional propellers in the configuration is of interest, considering the deformation described in this paper is asymmetric and extends far beyond the propeller radius. This would mean that adjacent slipstreams would be forced into an interaction due to the wing interference.

Acknowledgments

This work is partially funded by the Deutsche Forschungsgemeinschaft (DFG, German Research Foundation) under Germany's Excellence Strategy—EXC 2163/1—Sustainable and Energy Efficient Aviation—Project-ID 390881007. The authors acknowledge the use of ChatGPT 4.0 in the preparation of this document, solely to refine the language and improve the readability of the text. All content, ideas, and analyses presented in this paper are original works by the authors.

References

[1] Samuelsson, I., "Experimental Investigation of Low Speed Model Propeller Slipstream Aerodynamic Characteristics Including Flow Field Surveys and Nacelle/Wing Static Pressure Measurements," *17th Congress of the International Council of the Aeronautical Sciences*, International Council of the Aeronautical Sciences, Stockholm, Sweden, 1990, pp. 17–84, https://www.icas.org/icas_archive/ICAS1990/ICAS-90-3.1.3.pdf.

[2] Veldhuis, L., "Propeller Wing Aerodynamic Interference," Ph.D. Dissertation, Delft Univ. of Technology, Delft, The Netherlands, 2005, https://resolver.tudelft.nl/uuid:8ffbde9c-b483-40de-90e0-97095202fbe3.

[3] Felli, M., "Underlying Mechanisms of Propeller Wake Interaction with a Wing," *Journal of Fluid Mechanics*, Vol. 908, 2021, Paper A10. https://doi.org/10.1017/jfm.2020.792

[4] Duivenvoorden, R. R., Suard, N., Sinnige, T., and Veldhuis, L. L., "Experimental Investigation of Aerodynamic Interactions of a Wing with Deployed Fowler Flap Under Influence of a Propeller Slipstream," *AIAA Aviation 2022 Forum*, AIAA Paper 2022-3216, 2022. https://doi.org/10.2514/6.2022-3216

[5] Eshelby, M. E., "On the Aerodynamics of Installed Propellers," Paper 8 AGARD CP-366, Advisory Group for Aerospace Research and Development, 1984.

[6] Obert, E., *Aerodynamic Design of Transport Aircraft*, IOS Press, Amsterdam, The Netherlands, 2009, pp. 453–463. https://doi.org/10.3233/978-1-58603-970-7-i

[7] Prandtl, L., "Mutual Influence of Wings and Propeller," NACA TN 74, National Advisory Committee for Aeronautics, 1921, https://ntrs.nasa.gov/citations/19930080882.

[8] Jameson, A., "The Analysis of Propeller-Wing Flow Interaction," *NASA SP-228: Analytic Methods in Aircraft Aerodynamics*, National Aeronautics and Space Administration, 1970, pp. 721–742, https://ntrs.nasa.gov/citations/19700012077.

[9] Witkowski, D. P., Lee, A. K., and Sullivan, J. P., "Aerodynamic Interaction Between Propellers and Wings," *Journal of Aircraft*, Vol. 26, No. 9, 1989, pp. 829–836. https://doi.org/10.2514/3.45848

[10] Roosenboom, E. W., Heider, A., and Schröder, A., "Investigation of the Propeller Slipstream with Particle Image Velocimetry," *Journal of Aircraft*, Vol. 46, No. 2, 2009, pp. 442–449. https://doi.org/10.2514/1.33917

[11] Roosenboom, E. W., Stürmer, A., and Schröder, A., "Advanced Experimental and Numerical Validation and Analysis of Propeller Slipstream Flows," *Journal of Aircraft*, Vol. 47, No. 1, 2010, pp. 284–291. https://doi.org/10.2514/1.45961

[12] Roosenboom, E. W. M., "Image Based Measurement Techniques for Aircraft Propeller Flow Diagnostics," Ph.D. Dissertation, Delft Univ. of Technology, Delft, The Netherlands, 2011, https://resolver.tudelft.nl/uuid:c64eb373-9802-4eb4-bf9b-82a3811bbdd9.

[13] Kuhn, R. E., and Draper, J. W., "An Investigation of a Wing-Propeller Configuration Employing Large-Chord Plain Flaps and Large-Diameter Propellers for Low-Speed Flight and Vertical Take-Off," NACA TN 3307, National Advisory Committee for Aeronautics, 1954, https://ntrs.nasa.gov/citations/19930084052.

[14] Kuhn, R. E., "Investigation of Effectiveness of a Wing Equipped with a 50-Percent-Chord Sliding Flap, a 30-Percent-Chord Slotted Flap, and a 30-Percent-Chord Slat in Deflecting Propeller Slipstreams Downward for Vertical Take-Off," NASA Technical Memorandum, Vol. 3919, National Aeronautics and Space Administration, 1957, https://ntrs.nasa.gov/citations/19930084858.

[15] Hayes, W. C., Jr., Kuhn, R. E., and Sherman, I. R., "Effects of Propeller Position and Overlap on the Slipstream Deflection Characteristics of a Wing-Propeller Configuration Equipped with a Sliding and Fowler Flap," NACA TN 4404, National Advisory Committee for Aeronautics, 1958, https://ntrs.nasa.gov/citations/19930085249.

[16] Newsom, W. A., Jr., "Effect of Propeller Location and Flap Deflection on the Aerodynamic Characteristics of a Wing-Propeller Combination for Angles of Attack from 0 degrees to 80 degrees," NACA Technical Note, Vol. 3917, National Advisory Committee for Aeronautics, 1957, https://ntrs.nasa.gov/citations/19930084847.

[17] Felli, M., Roberto, C., and Guj, G., "Experimental Analysis of the Flow Field Around a Propeller–Rudder Configuration," *Experiments in Fluids*, Vol. 46, No. 1, 2009, pp. 147–164. https://doi.org/10.1007/s00348-008-0550-0

[18] Felli, M., and Falchi, M., "Propeller Tip and Hub Vortex Dynamics in the Interaction with a Rudder," *Experiments in Fluids*, Vol. 51, No. 5, 2011, pp. 1385–1402. https://doi.org/10.1007/s00348-011-1162-7

[19] Muscari, R., Dubbioso, G., and Di Mascio, A., "Analysis of the Flow Field Around a Rudder in the Wake of a Simplified Marine Propeller," *Journal of Fluid Mechanics*, Vol. 814, 2017, pp. 547–569. https://doi.org/10.1017/jfm.2017.43

[20] Posa, A., Broglia, R., and Balaras, E., "The Wake Structure of a Propeller Operating Upstream of a Hydrofoil," *Journal of Fluid Mechanics*, Vol. 904, No. A12, 2020, pp. 1–35. https://doi.org/10.1017/jfm.2020.680

[21] Posa, A., and Broglia, R., "Flow over a Hydrofoil at Incidence Immersed Within the Wake of a Propeller," *Physics of Fluids*, Vol. 33, No. 12, 2021. https://doi.org/10.1063/5.0075231

[22] Posa, A., and Broglia, R., "Development of the Wake Shed by a System Composed of a Propeller and a Rudder at Incidence," *International*

Journal of Heat and Fluid Flow, Vol. 94, 2022, Paper 108919. https://doi.org/10.1016/j.ijheatfluidflow.2021.108919

[23] Qiu, Y., Bai, J., and Qiao, L., "Aerodynamic Effects of Wing-Mounted Engine Nacelle on High-Lift Configuration of Turboprop Airliner," *Journal of Aircraft*, Vol. 55, No. 3, 2018, pp. 1082–1089. https://doi.org/10.2514/1.C034529

[24] van Arnhem, N., "Unconventional Propeller-Airframe Integration for Transport Aircraft Configurations," Ph.D. Dissertation, Delft Univ. of Technology, Delft, The Netherlands, 2022. https://doi.org/10.4233/uuid:4d47b0db-1e6a-4f38-af95-aafd33c29402

[25] Ribeiro, A. F., Duivenvoorden, R. R., and Martins, D., "High-Fidelity Simulations of Propeller-Wing Interactions in High-Lift Conditions," *AIAA Aviation 2023 Forum*, AIAA Paper 2023-3541, 2023. https://doi.org/10.2514/6.2023-3541

[26] Boermans, L., and Rutten, P., "Two-Dimensional Aerodynamic Characteristics of Airfoil NLF-MOD22 with Fowler Flap," Tech. Rept., Delft Univ. of Technology, Delft, The Netherlands, 1995. https://doi.org/10.5281/zenodo.13344026

[27] van Arnhem, N., de Vries, R., Sinnnige, T., and Veldhuis, L. L., "TUD-XPROP-S Propeller Geometry," Zenodo, Dataset, 2022. https://doi.org/10.5281/zenodo.6355670

[28] van Arnhem, N., de Vries, R., Sinnige, T., Vos, R., Eitelberg, G., and Veldhuis, L. L. M., "Engineering Method to Estimate the Blade Loading of Propellers in Nonuniform Flow," *AIAA Journal*, Vol. 58, No. 12, 2020, pp. 5332–5346. https://doi.org/10.2514/1.J059485

[29] Duivenvoorden, R. R., Sinnige, T., and Veldhuis, L. L. M., "Experimental Dataset of a Single Propeller-Wing-Flap Model (TUD-PWF) at Various Flap Deflections, Angles of Attack and Propeller Conditions," 4TU.ResearchData, Dataset, 2025. https://doi.org/10.4121/3161b813-ad38-4f9c-bb9d-333b895f46bc

[30] Duivenvoorden, R. R., de Vries, R., Sinnige, T., and Veldhuis, L. L. M., "TU Delft Propeller-Wing-Flap (TUD-PWF) Wind Tunnel Model Geometry," Zenodo, Dataset, 2025. https://doi.org/10.5281/zenodo.13344026

[31] Rumsey, C. L., Slotnick, J. P., and Sclafani, A. J., "Overview and Summary of the Third AIAA High Lift Prediction Workshop," *Journal of Aircraft*, Vol. 56, No. 2, 2019, pp. 621–644. https://doi.org/10.2514/1.C034940

[32] Smith, A. M. O., "High-Lift Aerodynamics," *Journal of Aircraft*, Vol. 12, No. 6, 1975, pp. 501–530. https://doi.org/10.2514/3.59830

[33] Stokkermans, T. C. A., and Veldhuis, L. L. M., "Propeller Performance at Large Angle of Attack Applicable to Compound Helicopters," *AIAA Journal*, Vol. 59, No. 6, 2021, pp. 2183–2199. https://doi.org/10.2514/1.J059509

[34] Cui, G.-P., Feng, L.-H., and Wang, W.-J., "Aerodynamic Characteristic of Deflected Slipstream Aimed at Vertical Takeoff and Landing," *Journal of Aircraft*, Vol. 56, No. 4, 2019, pp. 1418–1426. https://doi.org/10.2514/1.C035047

[35] Marshall, J. S., and Yalamanchili, R., "Vortex Cutting by a Blade. II - Computations of Vortex Response," *AIAA Journal*, Vol. 32, No. 7, 1994, pp. 1428–1436. https://doi.org/10.2514/3.12212

[36] Marshall, J. S., "Vortex Cutting by a Blade. I - General Theory and a Simple Solution," *AIAA Journal*, Vol. 32, No. 6, 1994, pp. 1145–1150. https://doi.org/10.2514/3.12113

[37] Marshall, J. S., and Grant, J. R., "Penetration of a Blade into a Vortex Core: Vorticity Response and Unsteady Blade Forces," *Journal of Fluid Mechanics*, Vol. 306, 1996, pp. 83–109. https://doi.org/10.1017/S0022112096001243

[38] Obert, E., "A Method for the Determination of the Effect of Propeller Slipstream on the Static Longitudinal Stability and Control of Multi-Engined Aircraft," Report LR-761, Delft Univ. of Technology, Delft, The Netherlands, 1994, https://repository.tudelft.nl/record/uuid:547ca83f-5b6b-4234-b580-b3cb82177294.

[39] Bouquet, T., and Vos, R., "Modeling the Propeller Slipstream Effect on Lift and Pitching Moment," *55th AIAA Aerospace Sciences Meeting*, AIAA Paper 2017-0236, 2017. https://doi.org/10.2514/6.2017-0236

J. Wang
Associate Editor